JM PAPERS

CrossMark

Effects of surface tension reduction on wind-wave growth and air–water scalar transfer

Keigo Matsuda[1,†], Satoru Komori[1,2], Naohisa Takagaki[3] and Ryo Onishi[1,4]

[1]Research Institute for Value-Added-Information Generation (VAiG), Japan Agency for Marine-Earth Science and Technology (JAMSTEC), Yokohama 236-0001, Japan

[2]High-Performance Fine-Particle Research Center, Doshisha University, Kyotanabe 610-0394, Japan

[3]Department of Mechanical Engineering, University of Hyogo, Himeji 671-2280, Japan

[4]Global Scientific Information and Computing Center, Tokyo Institute of Technology, Tokyo 152-8550, Japan

Effects of surface tension reduction on wind-wave growth are investigated using direct numerical simulations of air–water two-phase turbulent flows. The incompressible Navier–Stokes equations for air and water sides are solved using an arbitrary Lagrangian–Eulerian method with boundary-fitted moving grids. The wave growth of finite-amplitude and non-breaking gravity–capillary waves, whose wavelength is less than 0.07 m, is simulated for two cases of different surface tensions under a low-wind-speed condition of several metres per second. The results show that significant wave height for the smaller surface tension case increases faster than that for the larger surface tension case. Energy fluxes for gravity and capillary wave scales reveal that when the surface tension is reduced, the energy transfer from the significant gravity waves to capillary waves decreases, and the significant waves accumulate more energy supplied by wind. This results in faster wave growth for the smaller surface tension case. The effect on the scalar transfer across the air–water interface is also investigated. The results show that the scalar transfer coefficient on the water side decreases due to the surface tension reduction. The decrease is caused by suppression of turbulence in the water side. In order to support the conjecture, the surface tension effect is compared with laboratory experiments in a small wind-wave tank.

Key words: gas/liquid flow, wind-wave interactions

† Email address for correspondence: k.matsuda@jamstec.go.jp

K. Matsuda, S. Komori, N. Takagaki and R. Onishi

1. Introduction

Wind waves are generated by winds blowing over the air–water interface. A great number of studies have been published investigating the effects of wind waves on momentum, heat and mass transfers between the ocean and the atmosphere, which strongly affect the local and global weather and climate. In particular, the mass transfer across the air–water interface is an important issue for climate change studies because it is related to the air–sea CO_2 transfer (Wanninkhof *et al.* 2009). The study of the growth of wind waves also has a long history. The pioneering works on the theoretical aspect of the wind-wave growth were by Phillips (1957) and Miles (1957), and the understanding has been updated by a large number of analytical, experimental and numerical studies, including recent studies, e.g. Grare *et al.* (2013), Paquier, Moisy & Rabaud (2015, 2016), Zavadsky & Shemer (2017), Perrard *et al.* (2019), Buckley, Veron & Yousefi (2020) and Wu & Deike (2021). Sullivan & McWilliams (2010) and Wu & Deike (2021) reviewed and introduced the literature. While most published studies have considered wind waves on uncontaminated sea water or fresh water with constant surface tension, some studies have discussed the effects of surfactants on the wind-wave structure and have shown that wind waves are suppressed by the surfactants in water (Scott 1972; Mitsuyasu & Honda 1986). However, the detailed mechanism of the wind-wave suppression has not been confirmed. The mechanism of wind-wave suppression due to surfactants has been hypothesised based on the Marangoni effect. More specifically, the interface deformation is suppressed by the surface tension gradient on the interface, which is referred to as the Marangoni stress (e.g. Scott 1972). Non-uniform surfactant concentration on the free surface causes non-uniform surface tension distribution because the surface tension decreases as the surfactant concentration increases. However, this hypothesis is not proven since the Marangoni stress cannot be measured directly.

Furthermore, even in the case where surfactants are distributed uniformly on the free surface, the effect of uniform reduction of surface tension on the growth of wind waves remains unclear. Kawai (1979) discussed the cause of increase of the critical wind speed for soap water, considering the effect of uniform surface tension reduction. Kawai concluded analytically that the critical wind speed does not change significantly when the surface tension is reduced to half the value of water. Tsai & Lin (2004) suggested that uniform surface tension reduction increases the wind-wave growth rate based on linear stability analysis. However, this result can be applied only to the initial wave growth at very early stages. Zonta, Soldati & Onorato (2015) investigated the growth of gravity–capillary waves driven by the shear at the air–water interface using three-dimensional numerical simulation, and showed that the initial wave growth is faster for a larger Weber number (smaller surface tension). However, they did not clarify the pure surface tension effect because they changed both Froude and Weber numbers. Recently, Wu & Deike (2021) investigated numerically the fundamental mechanism of the growth of gravity–capillary waves with a laminar wind profile, changing the Bond and Reynolds numbers. However, they considered wind waves whose amplitude was smaller than the viscous sublayer thickness. Therefore, their two-dimensional simulation results cannot be applied directly to three-dimensional air–water flows involving turbulent eddies.

In addition, the dependence of uniform surface tension reduction on the mass transfer across the air–water interface is a subject of interest. Previous studies showed that the mass transfer is dominated by turbulence beneath the air–water interface (Komori, Nagaosa & Murakami 1993*a*; Komori *et al.* 2010). Veron & Melville (2001) showed that the effect of scalar transfer is affected by Langmuir circulations, which are streamwise vortices

developing below a wind-sheared air–water wavy interface. In contrast, Takagaki *et al.* (2015) performed direct numerical simulations (DNS) and concluded that the scalar transfer across a wind-driven air–water interface is mainly controlled by turbulent eddies, and the effect of the Langmuir circulations is relatively small. Recently, Tejada-Martínez *et al.* (2020) performed DNS and large-eddy simulations and reported that turbulence on the water side is triggered by the Langmuir forcing, whereas the intensity of the turbulence and the scalar transfer induced by the turbulence are driven by the wind shear. If the uniform surface tension changes the wave growth and the turbulence beneath the interface, then the mass transfer across the interface could be significantly affected by the surface tension.

This study aims to clarify the effects of uniform surface tension reduction on wind-wave growth and scalar transfer across the interface under a comparatively low wind speed condition of several metres per second, where intensive wave breaking does not occur. DNS of air–water two-phase flow are performed to investigate the effects of the surface tension reduction on the mechanism of the wave growth and air–water scalar transfer. In addition, the surface tension effects obtained by the DNS are discussed in Appendix A by comparing with the wave height measurements for aqueous solutions with different surface tensions in a small wind-wave tank.

2. Direct numerical simulations

2.1. *Computational method*

The governing equations for air and water flows are the continuity and Navier–Stokes equations for incompressible flows:

$$\frac{\partial U_i}{\partial x_i} = 0, \tag{2.1}$$

$$\frac{\partial U_i}{\partial t} + U_j \frac{\partial U_i}{\partial x_j} = -\frac{1}{\rho}\frac{\partial p}{\partial x_i} + \nu \frac{\partial^2 U_i}{\partial x_j \, \partial x_j} - g\delta_{i3}, \tag{2.2}$$

where U_i is the velocity component in the *i*th direction, p is the pressure, ρ is the density, ν is the kinematic viscosity, and g is the gravitational acceleration. Different values of ρ and ν were used for air and water flows: $\rho = \rho_a$ and $\nu = \nu_a$ for the air flow, and $\rho = \rho_w$ and $\nu = \nu_w$ for the water flow. The air–water interface was tracked by the height function $\eta(x_1, x_2)$, which represents the horizontal distribution of the vertical interface position. The transport equation of η is given by

$$\frac{\partial \eta}{\partial t} + U_1 \frac{\partial \eta}{\partial x_1} + U_2 \frac{\partial \eta}{\partial x_2} = U_3. \tag{2.3}$$

The dynamical balances at the interface in the normal and tangential directions are given by

$$p_w - \tau_{nw} + p_s = p_a - \tau_{na}, \tag{2.4}$$

$$\tau_{tw} = \tau_{ta}, \tag{2.5}$$

where the subscripts *a* and *w* represent the quantities in air and water, respectively. Here, τ_n and τ_t are the normal and tangential components of the viscous stress tensor on the interface, respectively; p_s is the pressure gap due to the surface tension σ and is given by $p_s = \sigma\kappa$, where κ is the interface curvature. The definition of the curvature κ is

summarised in Appendix B. The transport equation of the non-dimensional passive scalar C is given by

$$\frac{\partial C}{\partial t} + U_j \frac{\partial C}{\partial x_j} = D \frac{\partial^2 C}{\partial x_j \partial x_j}, \qquad (2.6)$$

where D is the diffusion coefficient of the scalar.

The governing equations were solved using an arbitrary Lagrangian–Eulerian (ALE) method with boundary-fitted moving grids (Komori *et al.* 1993*b*, 2010). The grid points were allowed to move in the vertical direction following interface deformation, while they were fixed in the horizontal direction. The grid points on the interface moved along with the vertical interface motion, and the vertical positions of the other grid points on the air and water sides were updated at each time step, adapting to the interface height change. The governing equations described on the Cartesian coordinate were transformed to the equations on the generalized coordinate and solved in separated domains for air and water flows; i.e. the density and viscosity for each flow were constant at each grid point. The detailed formulation of the ALE method used here is described in Komori *et al.* (1993*b*). The fifth-order upstream and fourth-order central finite difference schemes were adopted for the calculation of the advection and viscous terms, respectively. The velocity and pressure fields were coupled using the marker and cell (MAC) method. The time integration of each equation was calculated by the Euler implicit method. The reliability of the DNS code was confirmed using a comparison with laboratory experiment data (Komori *et al.* 1993*b*, 2010; Kurose *et al.* 2016).

As the interface shape is represented by the height function $\eta(x_1, x_2)$, the present DNS cannot consider the wave breaking with air entrainment or discontinuity of the surface slope. Occurrence of wave breaking can cause a numerical instability for (2.3). Deike and his colleagues (Deike, Popinet & Melville 2015; Deike, Melville & Popinet 2016; Mostert & Deike 2020; Wu & Deike 2021) performed DNS of two-phase flows with water waves using the volume of fluid (VOF) method with adaptive mesh refinement. Wave breaking can be captured by the VOF method explicitly. Here, we use the ALE method with boundary-fitted moving grids because breaking waves are not targeted. It should also be noted that the DNS of boundary-fitted approach in previous studies (Yang & Shen 2011; Zonta *et al.* 2015) used spectral methods for the spatial discretisation in the horizontal directions. The differentiations by finite difference schemes are less accurate than those by spectral methods for large wavenumbers, and the difference between the spectral and finite difference methods can be evaluated by the effective wavenumber k_{eff} (e.g. Ferziger, Perić & Street 2020). For the case of the finite difference schemes used in the present DNS, we confirmed that the difference between the effective wavenumber k_{eff} and the exact wavenumber k is less than 5 % for $k \leq 0.47 k_{max}$, where k_{max} is the maximum wavenumber and $k_{max} \approx 6.28 \times 10^3 \, \text{m}^{-1}$ for the present DNS. Therefore, the error in the present finite difference schemes is negligibly small for $k \lesssim 3.0 \times 10^3 \, \text{m}^{-1}$.

2.2. *Computational condition*

Figure 1 shows a schematic diagram of the computational domain. The domain size was set to $L_1 = 16\delta$, $L_2 = 3.84\delta$ and $L_3 = 3\delta$ in the streamwise (x_1), spanwise (x_2) and vertical (x_3) directions, respectively, where δ was set to $1.25 \times 10^{-2} \, \text{m}$. The initial interface was located 2δ above the bottom, and this height was set to $x_3 = 0$. The number of grid points was set to 400 in the streamwise direction, 96 in the spanwise direction, and 180 in the vertical direction (60 points on the air side and 120 points on the water side). The uniform grid spacing was used in streamwise and spanwise directions; i.e. the streamwise position
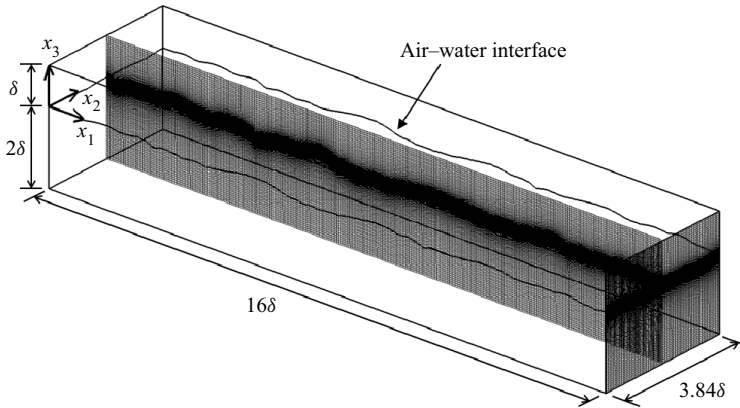
Figure 1. Schematic diagram of the computational domain and grids.

of the m_1th grid point is $x_g(m_1) = m_1 \Delta x_1$, and the spanwise position of the m_2th grid point is $y_g(m_2) = m_2 \Delta x_2$. The horizontal grid spacing is $\Delta x_1 = \Delta x_2 = 5.0 \times 10^{-4}$ m. In the vertical direction, the non-uniform grid spacing was adopted to set fine grids near the interface. As explained in the previous subsection, the vertical grid positions change depending on the interface height η; i.e. the vertical position of the m_3th grid point is given by $z_g(m_1, m_2, m_3) = -2\delta + \{\eta(x_g(m_1), y_g(m_2)) + 2\delta\} \zeta(M_w - m_3, M_w)$ for $m_3 = 0, \ldots, M_w$ (the water side and the interface), and $z_g(m_1, m_2, m_3) = \delta - \{\delta - \eta(x_g(m_1), y_g(m_2))\} \zeta(m_3 - M_w, M_a)$ for $m_3 = M_w + 1, \ldots, M_w + M_a$ (the air side), where $\zeta(m, M) = \tanh\{\alpha(1 - m/M)\}/\tanh\alpha$, and α is the scaling constant ($\alpha = 2.8$). Here, M_w and M_a are the numbers of vertical grid points in the water and air sides, respectively. When the interface is flat, i.e. $\eta(x_1, x_2) = 0$, the vertical position of the m_3th grid point is given by $z_{g0}(m_3) = -2\delta\{1 - \zeta(M_w - m_3, M_w)\}$ for $m_3 = 0, \ldots, M_w$, and $z_{g0}(m_3) = \delta\{1 - \zeta(m_3 - M_w, M_a)\}$ for $m_3 = M_w + 1, \ldots, M_w + M_a$. The minimum vertical grid spacings were 9.0×10^{-6} and 8.8×10^{-6} m in the air and water sides, respectively. These were sufficiently small to resolve the viscous sublayer thickness $\delta' \approx 5\nu/u_*$, which was 3.2×10^{-4} and 6.0×10^{-4} m for the air and water sides, respectively. The periodic boundary condition was applied to the velocity and pressure in the streamwise and spanwise directions, while the Neumann condition was applied in the vertical direction. A wall-bounded turbulent air flow had been developed for a flat and rigid surface until the velocity profile becomes a statistically steady state. The developed flow field was then used for the initial condition in the air side. The friction velocity on the air side was $u_{*a} \approx 0.24$ m s^{-1}. The corresponding free-stream wind speed was $U_\infty \approx 5.2$ m s^{-1} based on the empirical relationship of Iwano *et al.* (2013). The water side was initially in static condition, and the initial displacement of the interface was set to zero. A constant pressure gradient was applied to the air side in the streamwise direction for the driving force. The time integration was calculated for 7 seconds. The air and water densities were set to $\rho_a = 1.2$ kg m^{-3} and $\rho_w = 1.0 \times 10^3$ kg m^{-3}, respectively, and the kinematic viscosities in the air and water sides were set to $\nu_a = 1.5 \times 10^{-5}$ m^2 s^{-1} and $\nu_w = 1.0 \times 10^{-6}$ m^2 s^{-1}, respectively. The gravitational acceleration was set to $g = 9.8$ m s^{-2}. This study considers three cases of surface tension σ: (1) the case where the surface tension is equal to that of water ($\sigma = 1.0\sigma_w$), (2) the case where the surface tension is half that of water ($\sigma = 0.5\sigma_w$), and (3) the case where the surface tension is initially $\sigma = 1.0\sigma_w$ and suddenly reduced to

960 A22-5

$\sigma = 0.5\sigma_w$ at $t = 4.0$ s. The surface tension of water was set to $\sigma_w = 7.2 \times 10^{-2}$ N m^{-1}. We have confirmed the grid resolution dependence of the DNS results (Appendix C).

The friction Reynolds number is defined for each side of air and water using the friction velocity and the boundary layer thickness (δ_a and δ_w for the air and water sides, respectively). The friction Reynolds number on the air side, $Re_{\tau,a} = u_{*a}\delta_a/\nu_a$, is approximately 200, and it is sufficiently large to observe the logarithmic region. The friction Reynolds number on the water side, $Re_{\tau,w} = u_{*w}\delta_w/\nu_w$, is dependent on the time as the boundary layer develops along with the time. The DNS results show that for $t = 4.0$–7.0 s, $Re_{\tau,w}$ ranges from 165 to 193.

The scalar C represents the non-dimensional concentration of the imaginary absorbed gas. The scalar transport was calculated only in the water side because the concentration is uniform ($C = 1$) in the air side. The initial scalar concentration in the water side was set to 0, and the scalar concentration on the interface was fixed to $C = 1$ uniformly. The scalar transport calculation was started at $t = 4.0$ s, when wind waves were well developed. The Schmidt number, defined as $Sc \equiv \nu_w/D$, was set to $Sc = 1$ in the water side. Note that real gases usually have much larger Sc; e.g. $Sc \approx 600$ for CO_2. The scalar transfer coefficient k_L (which is defined in § 3.2 and also referred to as the transfer velocity) for such large Sc can be estimated from that for $Sc = 1$ using the relationship $k_L \propto Sc^{-1/2}$ (Jähne, Münnich & Siegenthaler 1979).

3. Results and discussion

3.1. *Effect on wave growth*

Figure 2 shows the shape of the air–water interface at $t = 6.0$ s for the water case (i.e. $\sigma = 1.0\sigma_w$) and the reduced surface tension case (i.e. $\sigma = 0.5\sigma_w$). The wind and the propagating waves move in the x_1 direction. For the case $\sigma = 1.0\sigma_w$, the wind waves form ripple waves on the downwind side of the wave crest. For the case $\sigma = 0.5\sigma_w$, the ripple waves are less significant than those for $\sigma = 1.0\sigma_w$, and the wave crests are slightly sharper. The above observation can be also confirmed by the streamwise distribution of instantaneous η at the middle position of the spanwise width ($x_2 = 2.4 \times 10^{-2}$ m) in figure 2(*c*). For $\sigma = 0.5\sigma_w$, the distribution of η in $0.1 \lesssim x_1 \lesssim 0.2$ m does not show clear ripple waves, while that for $\sigma = 1.0\sigma_w$ shows ripple-like interface fluctuations in the downwind side of the wave crest.

To quantify the effect of surface tension on the wave height, we have calculated the significant wave height H_s and the significant wavelength L_s (e.g. Toba 1972; Holthuijsen 2007). The significant waves are defined as the waves whose heights are the largest one-thirds among all individual waves, and the individual waves are identified using the zero-up crossing method (Pierson 1954; Takagaki *et al.* 2020). Here, H_s and L_s are the average wave height and wavelength of the significant waves, respectively. Figure 3 shows the temporal variations of H_s and L_s. Note that, as shown in figure 3(*b*), the significant waves do not capture wind waves at the initial period ($t \lesssim 1.0$ s) because the interface initially oscillates due to the initial impact of imposing the wall-bounded turbulent air flow driven by the pressure gradient. However, in the period $t = 1.0$–2.0 s, the wavelength is close to the minimum for both cases, and the wavelength for $\sigma = 0.5\sigma_w$ is slightly shorter than that for $\sigma = 1.0\sigma_w$. During and after this period, the significant wind waves are well captured, and their wavelengths for both σ cases remain less than or comparable to 0.07 m until $t = 7.0$ s. This means that the wind waves simulated in this study are classified as gravity–capillary waves ($0.004 \lesssim L_s \lesssim 0.07$ m) according to the classification in Lin *et al.* (2008). Figure 3(*a*) shows that after the significant waves capture wind waves, waves
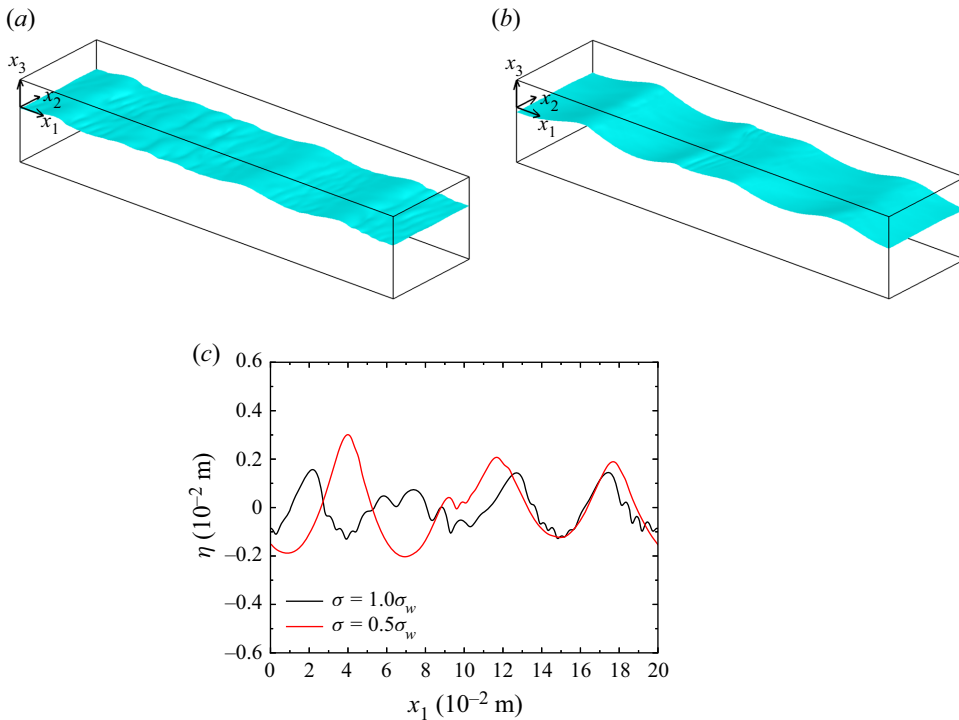
960 A22-6

Figure 2. Three-dimensional view of the air–water interface obtained by DNS for the cases (*a*) $\sigma = 1.0\sigma_w$ and (*b*) $\sigma = 0.5\sigma_w$, at $t = 6.0$ s. (*c*) Streamwise distribution of interface displacement η at $x_2 = 2.4 \times 10^{-2}$ m and $t = 6.0$ s.

for $\sigma = 0.5\sigma_w$ start growing earlier than $\sigma = 1.0\sigma_w$, and the wave height for $\sigma = 0.5\sigma_w$ is remarkably higher than that for $\sigma = 1.0\sigma_w$ after $t = 3.0$ s. This result means that the waves are not suppressed by the uniform surface tension reduction in contrast to the effect of surfactants. We have also confirmed the effect of uniform surface tension reduction on the wave height by conducting laboratory experiments using a small wind-wave tank (see Appendix A).

One could argue that the difference in wave height between the cases $\sigma = 1.0\sigma_w$ and $\sigma = 0.5\sigma_w$ in figure 3(*a*) is caused by hysteresis due to the difference in the initial wave development when the wind shear is loaded on the flat free surface. In order to clarify the dominance of hysteresis, we have performed the additional simulation with the surface tension suddenly changed to $\sigma = 0.5\sigma_w$ from the wind waves at $t = 4.0$ s developed using $\sigma = 1.0\sigma_w$. The results are shown by blue lines in figure 3. When the surface tension was changed to $\sigma = 0.5\sigma_w$, the significant wave height H_s becomes higher than in the case $\sigma = 1.0\sigma_w$, and becomes close to the case with the surface tension $\sigma = 0.5\sigma_w$ from the initial time ($t = 0$). This indicates that the hysteresis is not critical, whereas the wave growth speed is increased due to the surface tension reduction.

The surface tension dependence of the significant wavelength in the period $t = 1.0$–2.0 s is similar to the analytical result of the Kelvin–Helmholtz (K–H) instability, based on which the initial wavelength is given by $L_m \equiv 2\pi\sqrt{\gamma/g}$ (where $\gamma = \sigma/\rho_w$), which is the wavelength for minimum phase velocity. However, based on the theoretical analyses (Jeffreys 1925; Miles 1957, 1959), the classical K–H instability is not considered as the major mechanism that causes the initial wind-wave formation on an air–water interface.
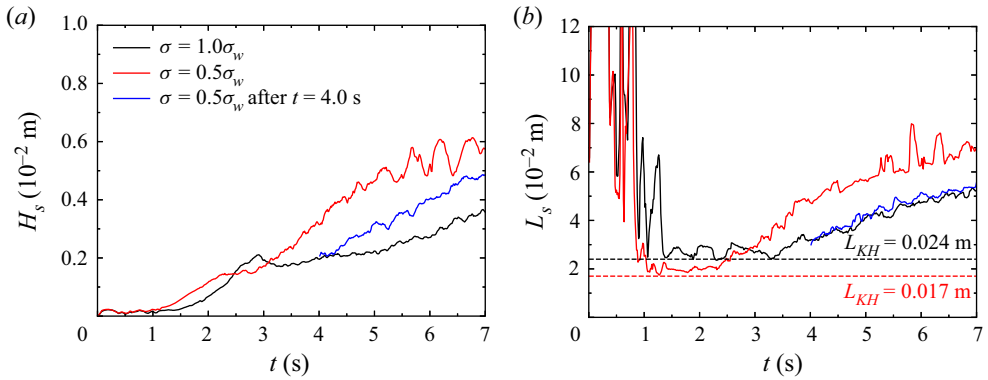
Figure 3. Temporal variations of (*a*) significant wave height H_s, and (*b*) significant wavelength L_s, for the cases $\sigma = 1.0\sigma_w$ and $\sigma = 0.5\sigma_w$, and a sudden change from $\sigma = 1.0\sigma_w$ to $\sigma = 0.5\sigma_w$ at $t = 4.0$ s. Dashed lines show the wavelength amplified by the weakly nonlinear Kelvin–Helmholtz instability L_{KH}.

Jeffreys (1925) and Miles (1957, 1993) proposed theoretical models for the formation of initial waves under turbulent winds. Their models estimate that the wave energy grows exponentially, and the initial wavelength formed at the minimum wind speed is approximately 0.06–0.08 m, where the effect of the surface tension is considered to be small. Miles' model is well accepted because the estimate agrees with observation data. However, this model cannot be applied to the present DNS results for the period $t = 1.0$–2.0 s. Miles (1957, 1993) considered the critical layer, which has the same mean wind speed as the wave speed, in the logarithmic layer of a wall-bounded turbulent flow, whereas in the present DNS results, the height for the wind speed equivalent to the wave speed is in the viscous sublayer. Miles (1959) generalized the K–H model to take into account the logarithmic layer of a wall-bounded turbulent flow, and concluded that the K–H instability is unlikely for air–water interfaces at commonly observed wind speeds. Apart from the initial wave formation, Bontozoglou & Hanratty (1990) examined the weakly nonlinear K–H instability (Miles 1986) to characterize the instability of finite-amplitude waves close to resonance, and showed that the K–H instability becomes strongly subcritical for the waves with wavelength shorter than the resonant wavelength given by $L_{KH} \equiv 2\pi\sqrt{2\gamma/g}$. They postulate that for air–water flows, gravity–capillary waves can be generated by winds and grow by the subcritical K–H instability so that those become sufficiently high to trigger a finite-amplitude bifurcation, doubling the wavelength (Chen & Saffman 1979, 1980). The resonant wavelengths L_{KH} for $\sigma = 1.0\sigma_w$ and $\sigma = 0.5\sigma_w$ are 0.024 m and 0.017 m, respectively. In the present DNS results for both surface tension cases, the significant wavelength L_s in the period $t = 1.0$–2.0 s almost corresponds to the wavelength L_{KH}. Therefore, we can conjecture that the waves in this period are amplified due to the subcritical K–H instability for finite-amplitude waves close to resonance.

The one-dimensional wave height spectrum $S_{\eta\eta}(k_1)$ in the streamwise direction has been calculated to understand the temporal change of H_s and L_s. The one-dimensional wave height spectrum is defined as $S_{\eta\eta}(k_1) \equiv (1/L_2) \int_0^{L_2} \hat{\eta}(k_1, x_2) \hat{\eta}^*(k_1, x_2) \, dx_2$, where $\hat{\eta}(k_1, x_2)$ is obtained by the Fourier transform in the streamwise direction, and k_1 is the streamwise wavenumber. An asterisk denotes the complex conjugate. Figure 4(*a*) shows the temporal change of the wave height spectrum for $\sigma = 1.0\sigma_w$. Note that the spectrum is temporally averaged for the past 0.5 s with respect to the indicated time instant. In the early growth period (up to $t = 2.5$ s), as predicted by Bontozoglou & Hanratty (1990), waves with wavenumbers close to and larger than $k_{KH} \equiv \sqrt{g/2\gamma} = 2\pi/L_{KH}$

grow predominantly. This is because the spectra for wavenumbers near k_{KH} and $2k_{KH}$ are amplified due to the subcritical K–H instability for the waves close to the second harmonic resonance at an early stage of wave growth (Bontozoglou & Hanratty 1990). After $t = 2.5$ s, the peak moves to a lower wavenumber as the wind waves grow, and the spectrum tail broadens on the high wavenumber side. The change of the peak location to lower wavenumbers corresponds to the increase in the significant wavelength in figure 3(*b*). The decrease of the peak wavenumber is commonly observed for wind waves (e.g. Imasato 1976), and these would be due to the nonlinear wave–wave interactions. The broadening of the spectrum tail on the high wavenumber side is due to a resonant nonlinear wave–wave interaction between the fundamental gravity wave and higher harmonics of order N, which forms ripple-like capillary waves (Chen & Saffman 1979; Fedorov, Melville & Rozenberg 1998; Caulliez 2013). The resonant condition can be satisfied approximately when the phase velocity of the capillary waves matches that of the fundamental wave. The wavenumber k_c of the capillary waves that resonate with the significant waves with wavenumber k_s is given by $k_c = k_m^2/k_s$, where $k_m = \sqrt{g/\gamma} = 2\pi/L_m$, when the nonlinearity is negligible. The arrows in figure 4(*a*) indicate the wavenumber $k_s = 2\pi/\overline{L_s}$ for the time-averaged significant wavelength $\overline{L_s}$ for $4.0 < t \leq 7.0$ s and the wavenumber k_c of the resonant capillary waves. The spectra at $t = 5.0$ and 7.0 s show a gentle slope for $k_m < k < k_c$ and decrease steeply for $k > k_c$. This confirms that the harmonic resonance causes the broadened spectrum. Figure 4(*b*) shows similar temporal change of the spectrum for $\sigma = 0.5\sigma_w$: even though k_{KH} for $\sigma = 0.5\sigma_w$ is larger than that for $\sigma = 1.0\sigma_w$ by a factor $\sqrt{2}$, waves with wavenumbers near k_{KH} grow predominantly in the early growth period (up to $t = 2.0$ s), and then the spectrum broadens on low and high wavenumber sides.

Figure 4(*c*) compares the wave height spectra for the two cases of surface tension. The spectra are temporally averaged over the period $4.0 < t \leq 7.0$ s. On the low-wavenumber side, the peak for $\sigma = 0.5\sigma_w$ is larger than that for $\sigma = 1.0\sigma_w$, corresponding to the larger significant wave height. On the high-wavenumber side, the wavenumber k_c of the resonant capillary waves increases due to the surface tension reduction because k_m is inversely proportional to the square root of the surface tension. The bump on the spectrum also moves to the higher wavenumber following the increase of k_c. This indicates that the wavelength of the resonant capillary waves becomes shorter. It is also observed that the amplitude at k_c for $\sigma = 0.5\sigma_w$ is approximately two orders of magnitude smaller than that for $\sigma = 1.0\sigma_w$. This means that ripple-like capillary waves are suppressed due to the surface tension reduction.

To understand the effect of surface tension reduction on the wind-wave growth mechanism, the potential energies due to gravity E_g and surface tension E_s were calculated using the equations

$$E_g = \frac{\rho_w g}{2L_1 L_2} \int_0^{L_1} \int_0^{L_2} \eta^2 \, dx_1 \, dx_2, \tag{3.1}$$

$$E_s = \frac{\sigma}{2L_1 L_2} \int_0^{L_1} \int_0^{L_2} \left\{ \left(\frac{\partial \eta}{\partial x_1}\right)^2 + \left(\frac{\partial \eta}{\partial x_2}\right)^2 \right\} \, dx_1 \, dx_2. \tag{3.2}$$

Figure 5 shows the temporal variations of E_g and E_s. The potential energies E_g and E_s are comparable in the early growth period $1.5 < t < 2.5$ s for $\sigma = 1.0\sigma_w$ and $1.0 < t < 2.0$ s for $\sigma = 0.5\sigma_w$. According to the small-amplitude linear wave theory, $E_g = E_s$ implies that the wavelength is equal to L_m. Figures 4(*a,b*) also show that waves with wavenumbers
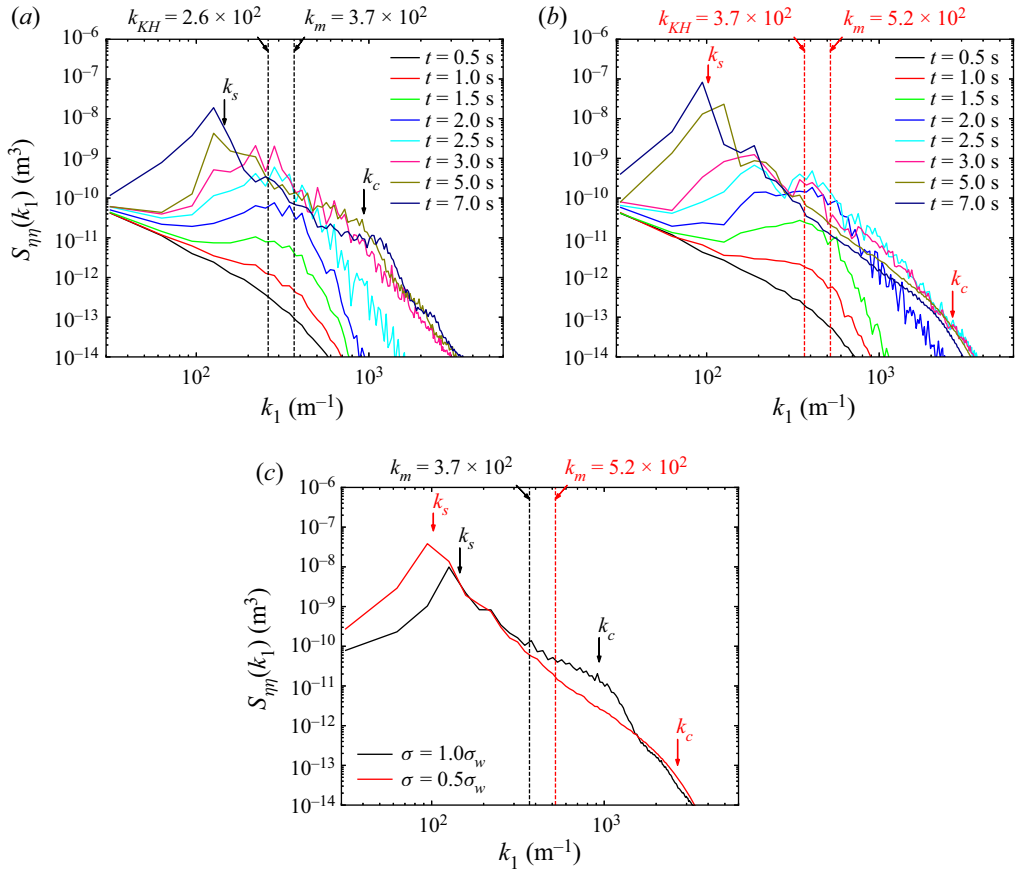
960 A22-9

Figure 4. Wave height spectra. Temporal evolutions of the spectra for (*a*) $\sigma = 1.0\sigma_w$ and (*b*) $\sigma = 0.5\sigma_w$ averaged for 0.5 s before the indicated time instant. (*c*) Comparison of spectra for $\sigma = 1.0\sigma_w$ and $\sigma = 0.5\sigma_w$ averaged for the period $4.0 < t \leq 7.0$ s. Dashed lines are the wavenumbers $k_{KH} = 2\pi/L_{KH}$ and $k_m = 2\pi/L_m$. The arrows indicate the wavenumber of the mean significant wave $k_s = 2\pi/\overline{L_s}$, and the resonant capillary wavenumber $k_c = k_m^2/k_s$, where $\overline{L_s}$ is the time-averaged L_s for the period 4.0–7.0 s. The wavenumbers for $\sigma = 1.0\sigma_w$ and $\sigma = 0.5\sigma_w$ are indicated in black and red, respectively.

near $k_{KH} \sim O(k_m)$ grow predominantly in the early growth period. This is also consistent with the fact that the significant wavelength in the early growth period is close to $L_{KH} = \sqrt{2}L_m$, as shown in figure 3(*b*). In the early growth period, the potential energy increases exponentially, and the energy growth rate for $\sigma = 0.5\sigma_w$ is larger than that for $\sigma = 1.0\sigma_w$. These results are qualitatively consistent with the results from the linear stability analysis of Tsai & Lin (2004). Lin *et al.* (2008) reported that, based on their DNS for air–water two-phase flows, initial linear wave growth is followed by exponential wave growth. In the present DNS results, only the later exponential growth is captured. After the early growth period, E_g increases, whereas E_s remains almost constant. The difference in the temporal variation between E_g and E_s corresponds to the broadening of the wave height spectra on both low- and high-wavenumber sides, as shown in figures 4(*a*,*b*). The surface potential energy E_s shows larger values for the larger surface tension as expected from the definition of E_s. In contrast, the potential energy E_g becomes larger for the smaller surface tension. The increase of E_g due to surface tension reduction is more significant than the decrease
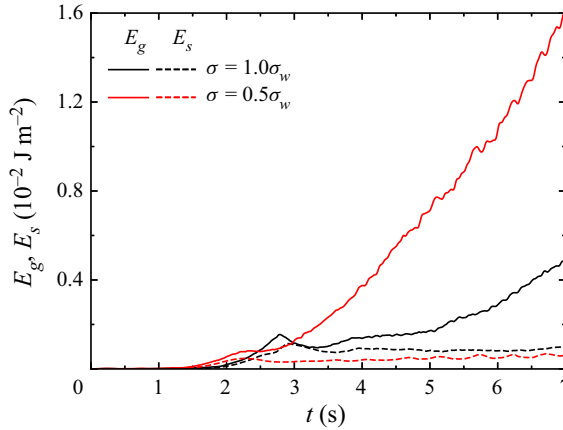
960 A22-10

Figure 5. Temporal variations of potential energies due to gravity and surface tension, E_g and E_s, for the cases $\sigma = 1.0\sigma_w$ and $\sigma = 0.5\sigma_w$.

of E_s. This also means that E_g increases faster for the smaller surface tension. It should be noted that Zavadsky & Shemer (2017) reported the temporal development of the wave height measured by applying nearly impulsive wind forcing. Their results show similar fast initial wave growth followed by the relatively slow wave growth. One would find that the growth of H_s becomes even gentler for $t > 5.0\,\mathrm{s}$ than for $t = 4.0$–$5.0\,\mathrm{s}$, while E_g for $\sigma = 0.5\sigma_w$ increases almost linearly with time for $t > 4.0\,\mathrm{s}$. Zavadsky & Shemer (2017) reported that the quasi-steady equilibrium state appears when the waves are long enough to be purely gravity waves, and this stage is considered as 'the principal stage' of Phillips (1957). Therefore, the gentler growth for $\sigma = 0.5\sigma_w$ at $t > 5.0\,\mathrm{s}$ could be relevant to this stage because the waves for $\sigma = 0.5\sigma_w$ are closer to pure gravity waves than the waves for $\sigma = 1.0\sigma_w$. However, clear transition to quasi-steady equilibrium state is not observed in the present DNS results.

To clarify the mechanism of faster increase of the potential energy E_g after the early growth period for the case of smaller surface tension in figure 5, we focus on the energy input from air to water and the energy dissipation in the water side. The energy fluxes due to the normal and tangential stress at the interface, Q_{na} and Q_{ta}, respectively, are given by

$$Q_{na} = \frac{1}{L_1 L_2} \int_{\Gamma} u_n (\tau_{na} - p_a - \rho_a g \eta) \, \mathrm{d}S, \tag{3.3}$$

$$Q_{ta} = \frac{1}{L_1 L_2} \int_{\Gamma} (u_{t1} \tau_{t1} + u_{t2} \tau_{t2}) \, \mathrm{d}S, \tag{3.4}$$

where u_n is the normal component of the interface velocity, and u_{t1} and u_{t2} are the tangential components of the interface velocity. Here, τ_{t1} and τ_{t2} are the tangential components of viscous stress in the directions of u_{t1} and u_{t2}, Γ represents the interface area, and $\mathrm{d}S$ is the infinitesimal area on Γ. Also, Q_{na} and Q_{ta} represent the energy fluxes per unit horizontal area, and can be considered as the energy fluxes attributed to the form and friction drags, respectively. It should be noted that in (3.3), we included the term $u_n \tau_{na}$, but its contribution was negligibly small. We have defined the energy dissipation rate in the water side per unit horizontal area, ϵ_w, as

$$\epsilon_w = \frac{1}{L_1 L_2} \int_{V_w} \epsilon \, \mathrm{d}V, \tag{3.5}$$
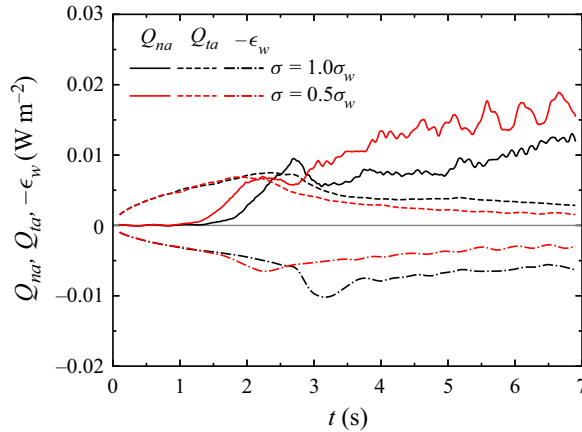
960 A22-11

Figure 6. Temporal variations of the energy fluxes due to the normal and tangential stresses, Q_{na} and Q_{ta}, and the energy dissipation rate ϵ_w in the water side as negative values. A simple centred moving average for the period 0.2 s is applied.

where the local energy dissipation rate ϵ is given by

$$\epsilon = 2\rho_w \nu_w s_{ij} s_{ij}, \tag{3.6}$$

in which s_{ij} is the (i, j) component of the strain-rate tensor, defined as $s_{ij} \equiv (\partial U_i/\partial x_j + \partial U_j/\partial x_i)/2$. In (3.5), V_w represents the volume in the water side.

Figure 6 shows the temporal variations of the energy fluxes from the air side to the water side, Q_{na} and Q_{ta}, as well as the energy dissipation rate on the water side, ϵ_w. The dissipation rate ϵ_w is shown as negative. A simple centred moving average for the period 0.2 s is applied. For $\sigma = 0.5\sigma_w$, Q_{na} is larger than that for $\sigma = 1.0\sigma_w$ except the period $2.4 \lesssim t \lesssim 2.9$ s, and Q_{ta} for $\sigma = 0.5\sigma_w$ becomes smaller than that for $\sigma = 1.0\sigma_w$ after $t \approx 1.9$ s. Both Q_{na} and Q_{ta} supply the kinetic energy to the water side, but Q_{ta} accelerates mainly the mean surface velocity and forms a shear layer under the interface. Whereas, Q_{na} contributes to the wave growth rather than Q_{ta} because the energy flux to gravity–capillary waves is attributed to the form drag (Melville & Fedorov 2015). Thus the larger values of Q_{na} for $\sigma = 0.5\sigma_w$ mean more energy input to the waves than in the case $\sigma = 1.0\sigma_w$. It should also be noted that the energy dissipation could also have a significant effect on the wave growth because steady gravity–capillary waves can be obtained when the energy flux due to the form drag is balanced by the viscous energy dissipation (Melville & Fedorov 2015). Figure 6 indicates that ϵ_w is not negligibly small compared to Q_{na}.

Therefore, we have examined the relationship between the energy fluxes and the rapid growth of E_g: the time derivative of E_g (i.e. dE_g/dt) has been compared with the energy input to waves and wave energy dissipation. Note that the energy dissipation rate ϵ_w also contains the dissipation due to mean shear, which does not contribute to the wave energy dissipation. Hence we consider the energy dissipation due to fluctuation of the strain rate, i.e. $\epsilon'_w \equiv \epsilon_w - \epsilon_{w,m}$, where $\epsilon_{w,m}$ is the energy dissipation rate due to the mean shear. We evaluated $\epsilon_{w,m}$ on the boundary-fitted coordinate as

$$\epsilon_{w,m} \equiv 2\rho_w \nu_w \int_{-2\delta}^{0} \langle s_{ij} \rangle_{z_{g0}} \langle s_{ij} \rangle_{z_{g0}} \, dz_{g0}, \tag{3.7}$$

where $\langle s_{ij} \rangle_{z_{g0}}$ is the horizontally averaged strain rate tensor for the same z_{g0}, i.e. the average over the surface $\Gamma_{z_{g0}}$, which initially locates at $x_3 = z_{g0}$ and moves along with the

960 A22-12
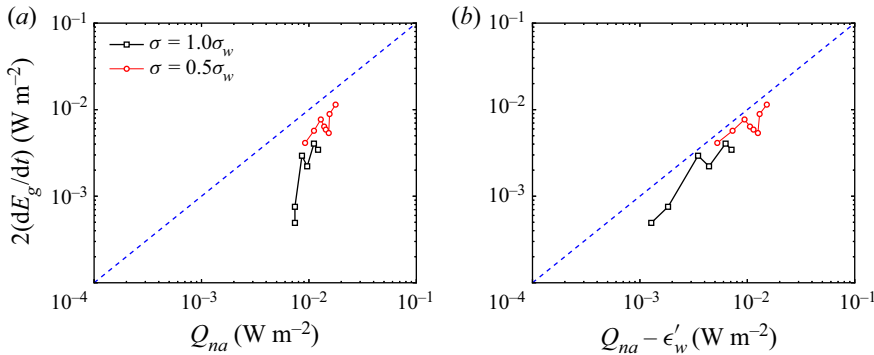
Figure 7. Wave energy change rate $2(\mathrm{d}E_g/\mathrm{d}t)$ against (*a*) Q_{na}, and (*b*) $Q_{na} - \epsilon'_w$. Here, Q_{na} and $Q_{na} - \epsilon'_w$ are temporally averaged for every 0.5 s after $t = 4.0$ s for $\sigma = 1.0\sigma_w$, and $t = 3.0$ s for $\sigma = 0.5\sigma_w$. We obtain $\mathrm{d}E_g/\mathrm{d}t$ by the linear fitting to E_g for every 0.5 s in the corresponding period.

boundary-fitted coordinate. Here, we used the approximation $\partial z_g/\partial z_{g0} \approx 1$ to calculate $\epsilon_{w,m}$: we assumed that the volume change at each grid is negligibly small. We have confirmed that the error of computing ϵ_w due to the approximation is negligibly small (less than 4 %). The time derivative $\mathrm{d}E_g/\mathrm{d}t$ has been calculated by fitting a linear function to the time series of E_g for every 0.5 s. Since we focused on the rapid growth of E_g, the change rate $\mathrm{d}E_g/\mathrm{d}t$ was calculated for $4.0 \leq t < 7.0$ s and $3.0 \leq t < 7.0$ s for $\sigma = 1.0\sigma_w$ and $\sigma = 0.5\sigma_w$, respectively. When the potential energy E_g increases, the kinetic energy associated with the gravity waves also increases, and the balance between energy input and dissipation should contribute to the increase of the total wave energy. However, it is difficult to extract the kinetic energy due to the wave motion from the total kinetic energy including the turbulent kinetic energy. Here, we assume that the kinetic energy of the waves is equivalent to the potential energy as it is the case of monochromatic waves. The change rate of the total energy of gravity waves is then given by $2(\mathrm{d}E_g/\mathrm{d}t)$. In figure 7, the change rate $2(\mathrm{d}E_g/\mathrm{d}t)$ for every 0.5 s is compared with the time-averaged Q_{na} and $Q_{na} - \epsilon'_w$ for every 0.5 s in the corresponding period. The dashed line indicates the $2(\mathrm{d}E_g/\mathrm{d}t)$ values equivalent to Q_{na} or $Q_{na} - \epsilon'_w$. In figure 7(*a*), the markers are located below the dashed line for both $\sigma = 1.0\sigma_w$ and $\sigma = 0.5\sigma_w$, meaning that the energy flux Q_{na} is larger than $2(\mathrm{d}E_g/\mathrm{d}t)$. In figure 7(*b*), the markers are also located below the dashed line, but closer to it. This means that the correlation of $2(\mathrm{d}E_g/\mathrm{d}t)$ with $Q_{na} - \epsilon'_w$ is better than that with Q_{na}. Thus the rapid growth of E_g is attributed to the energy flux due to normal stress Q_{na} minus the energy dissipation fluctuation ϵ'_w. The wave growth is often quantified by using the wave growth rate (Plant 1982; Donelan *et al.* 2006; Melville & Fedorov 2015), which is given by the change rate of the wave energy. The comparison of the wave growth rate obtained from the DNS results with the previous measurements is described in Appendix D.

The reason for the larger Q_{na} for $\sigma = 0.5\sigma_w$ is indeed not surprising because Q_{na} is the energy flux attributed to the form drag, and it is reasonable to assume that the form drag becomes larger along with wave growth. The form drag D_p is given by

$$D_p = \frac{1}{L_1 L_2} \int_\Gamma (p_a + \rho_a g\eta)n_1 \, \mathrm{d}S, \tag{3.8}$$

where n_1 is the streamwise component of the normal vector to the interface. Melville & Fedorov (2015) evaluated the energy flux due to the normal stress by $Q_{na} \approx \mathcal{C}D_p$, where
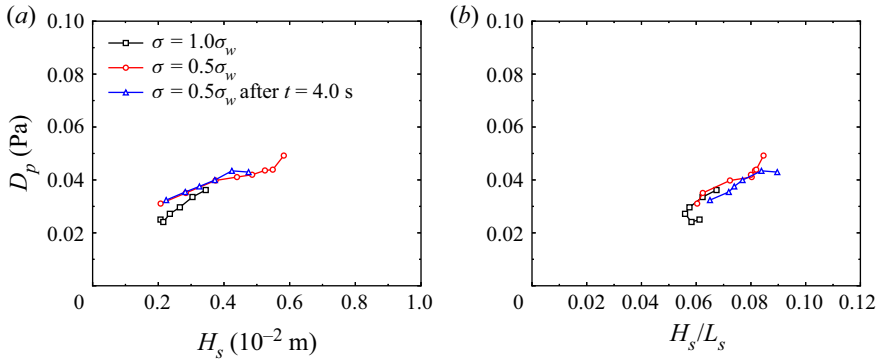
Figure 8. Form drag D_p against (a) significant wave height H_s, and (b) wave slope H_s/L_s. Here, D_p, H_s and H_s/L_s are temporally averaged for every 0.5 s after $t = 4.0$ s for $\sigma = 1.0\sigma_w$, and $t = 3.0$ s for $\sigma = 0.5\sigma_w$.

$\mathcal{C}$ is the wave velocity. We have confirmed that Q_{na} and $\mathcal{C}D_p$ are well correlated also in our results. Here, the obtained form drag D_p is compared with the significant wave height H_s and the wave slope H_s/L_s in figure 8. Similar to figure 7, the time-averaged values for every 0.5 s are plotted for $4.0 \le t < 7.0$ s and $3.0 \le t < 7.0$ s for $\sigma = 1.0\sigma_w$ and $\sigma = 0.5\sigma_w$, respectively. In figure 8(a), the form drag D_p for the same wave height H_s is larger for the smaller surface tension case. The difference in D_p between the cases $\sigma = 1.0\sigma_w$ and $\sigma = 0.5\sigma_w$ is robust because D_p calculated for the case of sudden change from $\sigma = 1.0\sigma_w$ to $\sigma = 0.5\sigma_w$ at $t = 4.0$ s also becomes larger than D_p for the case where the surface tension remained $\sigma = 1.0\sigma_w$. Figure 8(b) shows that the form drag D_p is rather correlated with the wave slope H_s/L_s because D_p for the three cases of surface tension well collapse. This means that the significant waves become steeper due to the surface tension reduction, and that causes the increases of the form drag D_p. Therefore, the increase of Q_{na} due to the surface tension reduction can be explained by the increase of the wave slope H_s/L_s.

To investigate the relationship between the energy fluxes and the surface tension, we have evaluated the energy fluxes for the gravity and capillary waves separately. Here, the energy fluxes due to the normal stress at gravity and capillary wave scales ($Q_{na,g}$ and $Q_{na,c}$, respectively) are defined as

$$Q_{na,g} = \int_0^{k_{cut}} S_{Qna}(k)\, \mathrm{d}k, \tag{3.9}$$

$$Q_{na,c} = \int_{k_{cut}}^{k_{max}} S_{Qna}(k)\, \mathrm{d}k, \tag{3.10}$$

where k is the magnitude of the two-dimensional horizontal wavenumber vector $\boldsymbol{k} = (k_1, k_2)$, k_{max} is the maximum wavenumber, and $S_{Qna}(k)$ is the Fourier spectrum of the energy flux due to the normal stress at the interface. This $S_{Qna}(k)$ can be given by

$$S_{Qna}(k) = \frac{1}{\Delta k} \sum_{k-\Delta k/2 \le |\boldsymbol{k}| < k+\Delta k/2} \mathrm{Re}\left[-\widehat{(p_a + \rho_a g\eta)}\, \frac{\widehat{\partial\eta}^*}{\partial t} \right], \tag{3.11}$$

where $\hat{A}(k_1, k_2)$ indicates the Fourier coefficient of a given horizontal distribution $A(x_1, x_2)$, and $\mathrm{Re}[\cdot]$ indicates the real part of the complex number. We can interpret $Q_{na,g}$ and $Q_{na,c}$ as sharp-cut low- and high-pass filtered values of local energy flux

960 A22-14

$-(p_a + \rho_a g \eta)(\partial \eta / \partial t)$ for the cut-off wavenumber k_{cut}. We set k_{cut} to k_m for $\sigma = 1.0\sigma_w$. We have confirmed that the above energy fluxes satisfy $Q_{na} = Q_{na,g} + Q_{na,c}$. Similarly, the energy dissipation at gravity and capillary wave scales, $\epsilon_{w,g}$ and $\epsilon_{w,c}$, respectively, are defined as

$$\epsilon_{w,g} = \int_0^{k_{cut}} \int_{-2\delta}^0 S_{\epsilon w}(k, z_{g0}) \, dz_{g0} \, dk, \tag{3.12}$$

$$\epsilon_{w,c} = \int_{k_{cut}}^{k_{max}} \int_{-2\delta}^0 S_{\epsilon w}(k, z_{g0}) \, dz_{g0} \, dk, \tag{3.13}$$

where $S_{\epsilon w}(k, z_{g0})$ is the Fourier spectrum of the energy dissipation rate as a function of initial vertical position z_{g0}. Here, $S_{\epsilon w}(k, z_{g0})$ can be given by

$$S_{\epsilon w}(k, z_{g0}(m_3)) = \frac{2\rho_w \nu_w}{\Delta k} \sum_{k - \Delta k/2 \le |\mathbf{k}| < k + \Delta k/2} \text{Re} \left[\widehat{s}_{ij}(\mathbf{k}, z_{g0}(m_3)) \, \widehat{s}_{ij}^*(\mathbf{k}, z_{g0}(m_3)) \right], \tag{3.14}$$

where $\widehat{s}_{ij}(\mathbf{k}, z_{g0}(m_3))$ is obtained by the Fourier transform in the x_1 and x_2 directions for $s_{ij}(x_g(m_1), y_g(m_2), z_g(m_1, m_2, m_3))$ for each m_3. We used the approximation $\partial z_g / \partial z_{g0} \approx 1$ again to define $\epsilon_{w,g}$ and $\epsilon_{w,c}$ as (3.12) and (3.13), respectively. We have confirmed that sum of these energy dissipation rates is approximately equal to ϵ_w'; i.e. $\epsilon_{w,g} + \epsilon_{w,c} \approx \epsilon_w'$.

Figure 9 shows the energy flux due to normal stress and the energy dissipation rate at gravity and capillary wave scales. After $t = 2.5$ s, $Q_{na,g}$ is larger than $Q_{na,c}$, indicating that the energy flux due to the normal stress at the gravity wave scales has dominant influence on the total energy flux Q_{na}. This is consistent with our intuition that the contribution of the form drag is dominated by the significant gravity waves. Concerning the dissipation rate, $\epsilon_{w,c}$ is far larger than $\epsilon_{w,g}$. Therefore, the energy dissipation at the capillary wave scales is dominant for ϵ_w'. The energy dissipation for capillary wave scales $\epsilon_{w,c}$ for $\sigma = 1.0\sigma_w$ is significantly larger than that for $\sigma = 0.5\sigma_w$. It is also observed in figure 9(*b*) that $\epsilon_{w,c}$ is larger than $Q_{na,c}$. This means that the energy dissipation in the water side exceeds the energy input from the air side at the capillary wave scales, and there must be energy transfer from the gravity wave scales to the capillary wave scales. The difference between $\epsilon_{w,c}$ and $Q_{na,c}$ is smaller for the smaller surface tension case. This indicates that the energy transfer from the gravity wave scales decreases due to the surface tension reduction. There are several mechanisms that can result in the inter-scale energy transfer: the four-wave resonant interaction, harmonic resonance of nonlinear waves, and turbulent energy transfer. Unfortunately, it is difficult to specify the dominant mechanism because of the difficulty of evaluating the energy transfer. However, comparison of Q_{ta} (in figure 6) and $\epsilon_{w,c}$ suggests that change in the resonant condition due to the surface tension reduction results in the decrease of the energy transfer from the gravity wave scales because $\epsilon_{w,c}$ (i.e. the energy transfer from the gravity wave scales) is larger than Q_{ta}, which produces shear-induced turbulence in the water side, for $\sigma = 1.0\sigma_w$.

To fully understand the wave growth mechanism, quantitative evaluation of wave–wave interaction is crucial. However, it is difficult to evaluate the energy flux between waves directly from our simulation data. The present results of the energy fluxes at gravity and capillary wave scales indirectly prove the energy transfer between these scales and the effect of the surface tension reduction on the energy transfer. These results indicate that the significant gravity waves receive kinetic energy from the air side with contributions of form drag, i.e. Q_{na}, and the energy is partially transferred to capillary waves and dissipated by the viscosity of water. When the surface tension decreases, the energy transfer to the
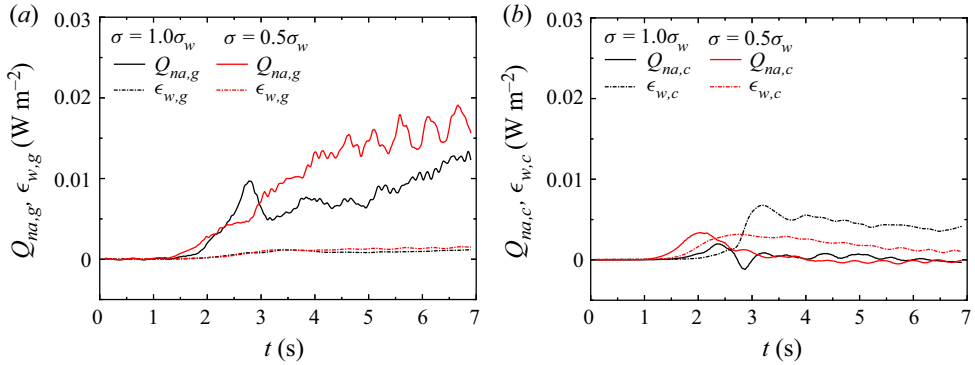
Figure 9. Energy flux due to normal stress and energy dissipation rate at (*a*) gravity wave scales and (*b*) capillary wave scales. A simple centred moving average for the period 0.2 s is applied.

capillary waves decreases, and the significant waves retain more energy, resulting in the faster growth of the wave height. The faster wave growth can further cause the increase in the wave slope, and therefore the increase of the energy received from the air side with contributions of form drag.

3.2. *Effect on scalar transfer*

The effect of the surface tension reduction on the scalar transfer across the air–water interface has been investigated by solving the scalar transport equation (2.6) for $t \geq 4.0$ s. The scalar transfer was evaluated by the scalar transfer coefficient in the water side k_L, defined as

$$F = k_L(C_i - C_b). \tag{3.15}$$

Here, C_i is the scalar concentration on the interface ($C_i = 1$), C_b is the bulk scalar concentration on the water side ($C_b = 0$), and F is the horizontally averaged scalar flux defined as

$$F = \frac{1}{L_1 L_2} \int_\Gamma D \frac{\partial C}{\partial x_n} \, dS, \tag{3.16}$$

where x_n is the normal distance from the interface. Figure 10 shows the scalar transfer coefficient k_L for $\sigma = 1.0\sigma_w$ and $0.5\sigma_w$. Immediately after the start of the scalar transport calculation at $t = 4.0$ s, k_L shows large values because a large concentration gradient near the air–water interface is formed in this transient period. However, for $t > 4.5$ s, the scalar concentration boundary layer is sufficiently developed to achieve the local equilibrium of scalar transfer near the interface, and k_L for $\sigma = 0.5\sigma_w$ is smaller than that for $\sigma = 1.0\sigma_w$. That is, the scalar transfer decreases as the surface tension decreases. The difference is approximately 6.5 % for $5.0 \leq t \leq 7.0$ s. One could postulate that the decrease of k_L is due to the difference in the surface area of the air–water interface. Figure 11 shows the temporal variation of the surface area expansion ratio, defined as the ratio of the surface area of the interface to the horizontal area. The change in the expansion ratio is less than or approximately equal to 2 %, and the difference of the expansion ratio is even smaller; i.e. the difference of the expansion ratio is too small to explain the difference of k_L. These results indicate that the difference in the surface area of the interface does not explain the 6.5 % decrease in k_L due to the surface tension reduction.

The transfer of gases such as CO_2 across a wind-driven wavy air–water interface is strongly affected by the turbulence under the interface (Komori *et al.* 1993*a*).
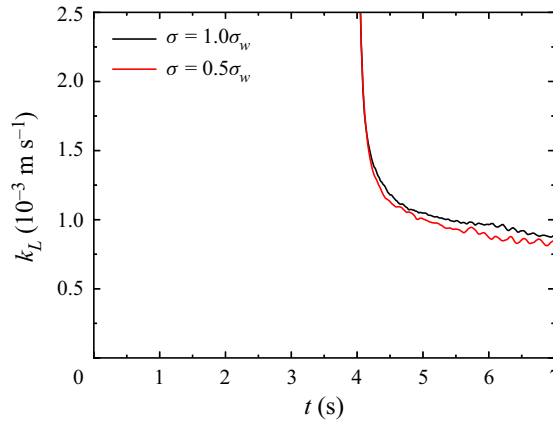
960 A22-16

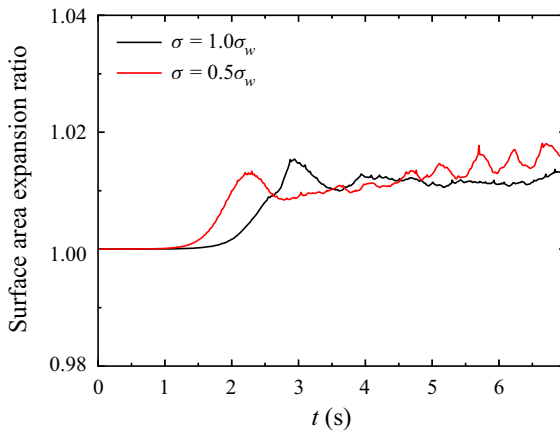Figure 10. Temporal variations of scalar transfer coefficient k_L on the water side.

Figure 11. Temporal variations of surface area expansion ratio.

Figures 12(a,b) show the local scalar flux $F_{local} \equiv D(\partial C/\partial x_n)$ on the interface. The colour contours on the side walls show the scalar concentration in the water side. For the case $\sigma = 1.0\sigma_w$ in figure 12(a), there are streamwise streaky structures of the local scalar flux on the interface, which are formed due to the turbulent flow structure in the water side (Komori *et al.* 2010; Takagaki *et al.* 2015; Tejada-Martínez *et al.* 2020). The similar streaky structures of the local scalar flux are also observed for the case $\sigma = 0.5\sigma_w$ in figure 12(b), suggesting that the turbulence significantly affects the scalar transfer even when the surface tension is reduced.

To evaluate the scalar transfer below the moving interface, we calculate the downward scalar flux on the continuous surface $\Gamma_{z_{g0}}$, introduced in § 3.1. The surface $\Gamma_{z_{g0}}$ can also be considered as the surface for a fixed vertical index m_3, and the surface $\Gamma_{z_{g0}}$ for $z_{g0} = 0$ corresponds to the air–water interface Γ. The scalar budget is evaluated for the volume below the surface $\Gamma_{z_{g0}}$. The scalar budget equation can be described for each level of z_{g0} as

$$\frac{\mathrm{d}\chi(z_{g0})}{\mathrm{d}t} = F_{diff}(z_{g0}) + F_{turb}(z_{g0}),$$ (3.17)
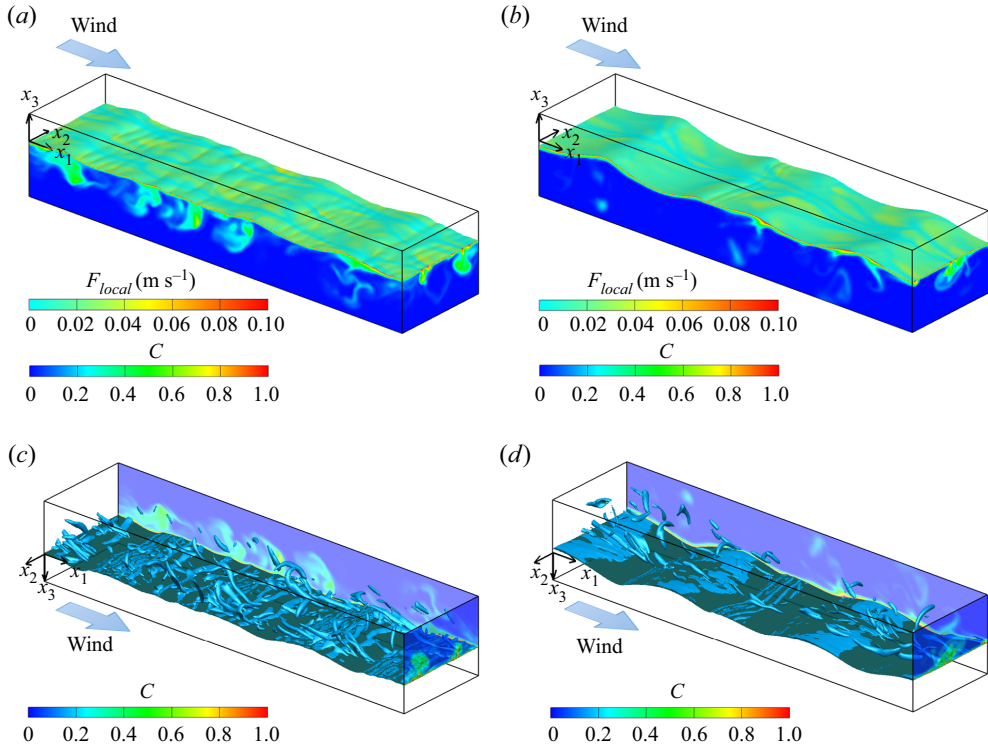
960 A22-17

Figure 12. (*a,b*) Colour contours of the local scalar flux F_{local} on the interface at $t = 6.0$ s. (*c,d*) Isosurfaces of the second invariant of velocity gradient tensor ($Q = 0.002 \text{ s}^{-2}$) in the water side, viewed from the water side (bottom side up), at $t = 6.0$ s. Here, (*a,c*) $\sigma = 1.0\sigma_w$, and (*b,d*) $\sigma = 0.5\sigma_w$. The colour contours on the side walls show the scalar concentration C.

where $\chi(z_{g0})$ is the total scalar per unit horizontal area integrated for the volume below the surface $\Gamma_{z_{g0}}$, and $F_{diff}(z_{g0})$ and $F_{turb}(z_{g0})$ are the downward molecular diffusion and turbulent scalar fluxes across the surface $\Gamma_{z_{g0}}$, respectively. Here, $\chi(z_{g0})$, $F_{diff}(z_{g0})$ and $F_{turb}(z_{g0})$ are defined as

$$\chi(z_{g0}) = \frac{1}{L_1 L_2} \int_0^{L_1} \int_0^{L_2} \left\{ \int_{-2\delta}^{z(x_1, x_2, z_{g0})} C \, dx_3 \right\} dx_1 \, dx_2, \tag{3.18}$$

$$F_{diff}(z_{g0}) = \frac{1}{L_1 L_2} \int_{\Gamma_{z_{g0}}} D \frac{\partial C}{\partial x_j} n_j \, dS_{z_{g0}}, \tag{3.19}$$

$$F_{turb}(z_{g0}) = - \langle c w_3 \rangle_{z_{g0}}, \tag{3.20}$$

where $z(x_1, x_2, z_{g0})$ is the vertical position of the surface $\Gamma_{z_{g0}}$, n_j is the jth component of the unit normal vector to $\Gamma_{z_{g0}}$, $dS_{z_{g0}}$ is the infinitesimal area on $\Gamma_{z_{g0}}$, c is the scalar concentration fluctuation ($c \equiv C - \langle C \rangle_{z_{g0}}$), w_3 is the vertical fluid velocity relative to the velocity of the boundary-fitted coordinate ($w_3 \equiv U_3 - U_1(\partial z_g/\partial x_1) - U_2(\partial z_g/\partial x_2) - V_3$, where $V_3 = \partial z_g/\partial t$ is the vertical velocity of the boundary-fitted coordinate), and the brackets $\langle \cdot \rangle_{z_{g0}}$ denote the horizontal average over the surface $\Gamma_{z_{g0}}$, i.e. $\langle A \rangle_{z_{g0}} = (1/L_1 L_2) \int_0^{L_1} \int_0^{L_2} A(x_1, x_2, z(x_1, x_2, z_{g0})) \, dx_1 \, dx_2$ for a given function A. The derivation of the scalar budget equation (3.17) is described in Appendix E.
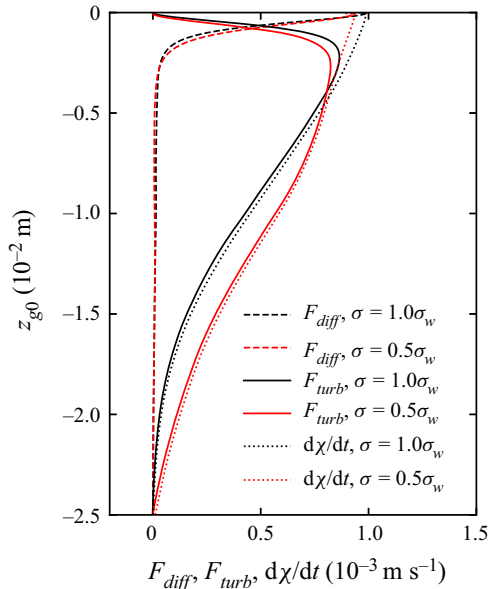
960 A22-18

Figure 13. Vertical profiles of downward molecular diffusion and turbulent scalar fluxes, F_{diff} and F_{turb}, respectively, and the time change of stored scalar χ below z_{g0}. The temporal average was taken for the period $5.0 \leq t \leq 7.0\,\mathrm{s}$. The horizontal average was taken on the boundary-fitted coordinate.

Figure 13 shows the vertical profiles of the downward molecular diffusion and turbulent scalar flux, F_{diff} and F_{turb}, respectively, and the time change of χ. The temporal average is taken for the period $5.0 \leq t \leq 7.0\,\mathrm{s}$, while the scalar budget equation (3.17) is described for instantaneous scalar distribution. For both cases $\sigma = 1.0\sigma_w$ and $\sigma = 0.5\sigma_w$, F_{diff} is dominant for the scalar transfer only near the air–water interface. The profile of F_{turb} shows a peak at $z_{g0} \approx -2.2 \times 10^{-3}\,\mathrm{m}$, and F_{turb} is dominant below this vertical location. The peak value of F_{turb} for $\sigma = 0.5\sigma_w$ is approximately 4.7 % smaller than that for $\sigma = 1.0\sigma_w$. The magnitude and the difference of the peak values are consistent with the difference in $\mathrm{d}\chi/\mathrm{d}t$ near the surface and the difference in k_L in figure 10. These results indicate that the decrease in k_L due to surface tension reduction is caused by the decrease in the turbulent scalar transfer.

In figure 6, it is observed that Q_{ta} for $\sigma = 0.5\sigma_w$ is smaller than that for $\sigma = 1.0\sigma_w$. This means that the energy input for the shear-induced turbulence weakens due to the surface tension reduction. To confirm the turbulence structures in the water side, the turbulent vortices have been visualised by using the second invariant of the velocity gradient tensor, $Q \equiv (\omega_{ij}\omega_{ij} - s_{ij}s_{ij})/2$, where ω_{ij} is the vorticity tensor defined as $\omega_{ij} \equiv (\partial U_j/\partial x_i - \partial U_i/\partial x_j)/2$, and s_{ij} is the strain-rate tensor defined above. Figures 12(c,d) show isosurfaces of $Q = 0.002\,\mathrm{s}^{-2}$, viewed from the water side (bottom side up). Strong turbulent vortices are distributed near the interface for both surface tension cases: spanwise vortices are observed in the vicinity of the interface, and streamwise vortices are observed below the wave troughs. The structure similar to the spanwise vorticity was reported by Hung & Tsai (2009). They computed the evolution of two-dimensional gravity–capillary waves and observed that vortices shed from wave troughs distribute in the vicinity of the interface. The streaky structure of the scalar flux on the interface is attributed to trains of the streamwise vortices. It is also observed that the streamwise vortices for $\sigma = 0.5\sigma_w$ are less than those for $\sigma = 1.0\sigma_w$.
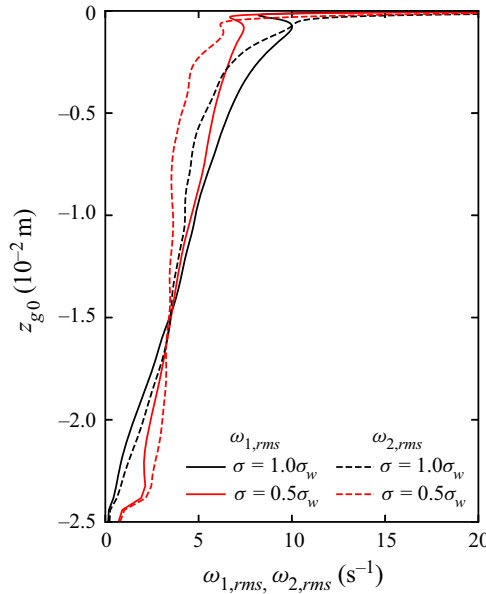
Figure 14. Vertical profiles of root mean square (r.m.s.) values for streamwise and spanwise vorticity fluctuations, $\omega_{1,rms}$ and $\omega_{2,rms}$, respectively. The temporal average was taken for the period $5.0 \leq t \leq 7.0$ s.

To compare the turbulent fluctuations, we have calculated the root mean square (r.m.s.) values of the streamwise and spanwise vorticities, because it is difficult to separate the effects of wave motion and turbulent flow on the velocity fluctuation. Figure 14 shows the r.m.s. values of streamwise and spanwise vorticity fluctuations, $\omega_{1,rms}$ and $\omega_{2,rms}$, respectively. Large values of $\omega_{1,rms}$ and $\omega_{2,rms}$ are observed in the vicinity of the interface, and these large values correspond to the spanwise vortices in figures 12(*c*,*d*). At the vertical position of $z_{g0} \approx -2.2 \times 10^{-3}$ m, where the peak of F_{turb} is located, the streamwise vorticity fluctuation $\omega_{1,rms}$ exceeds the spanwise vorticity fluctuation $\omega_{2,rms}$. Thus the streamwise vortices play major roles for the turbulent scalar transfer quantified by F_{turb}. We can also find that the streamwise vorticity fluctuation is weaker for the case $\sigma = 0.5\sigma_w$. This also indicates that the decrease in the turbulent scalar transfer is due to the decrease in the turbulent fluctuation. The shear in the water side is produced by the energy flux Q_{ta}, as explained above. Thus the smaller Q_{ta} can result in the weaker shear-induced turbulence. The decrease of Q_{ta} is attributed to the decrease of the friction drag. Note that the friction and form drags satisfy the relationship $D_f + D_p = \rho_a u_{*a}^2 \approx$ const., where D_f and D_p are the friction and form drags, respectively, with D_p given by (3.8), and D_f given by

$$D_f = \frac{1}{L_1 L_2} \int_\Gamma \tau_{ta} t_1 \, \mathrm{d}S, \tag{3.21}$$

where t_1 is the streamwise component of the tangential vector to the interface. Figure 15 shows the friction and form drags, D_f and D_p. For $t \geq 4.0$ s, the form drag D_p increases with time, and D_p for the case of smaller surface tension is larger than that for the larger surface tension. As discussed in the previous subsection, the increase in D_p is attributed to the increase in the wave slope H_s/L_s associated with the wave growth. In contrast, the friction drag D_f decreases with time, and D_f for the smaller surface tension case is
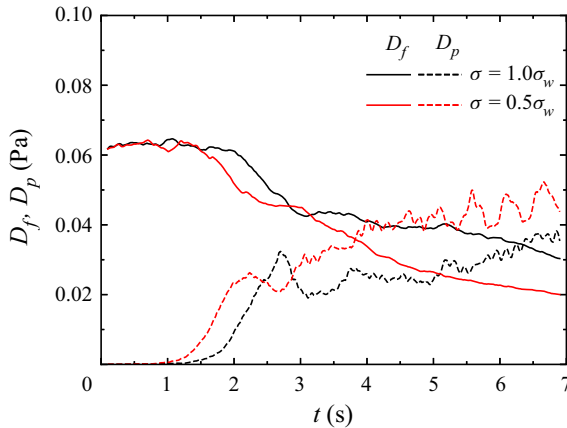
960 A22-20

Figure 15. Temporal variations of friction and form drags, D_f and D_p. A simple centred moving average for the period 0.2 s is applied.

smaller than that for the larger surface tension. This suggests that the shear-induced water turbulence, which promotes the scalar transfer across the interface, can be suppressed by the decrease in D_f due to the surface tension reduction.

These results indicate that when the surface tension is reduced, the wind wave becomes higher and the surface area becomes slightly larger. However, the scalar transfer across the air–water interface decreases because the turbulence under the interface is suppressed due to the decrease in the friction drag.

4. Conclusions

Effects of uniform surface tension reduction on the wind-wave growth and the scalar transfer across the air–water interface have been investigated for finite-amplitude and non-breaking gravity–capillary waves using direct numerical simulations (DNS) of wind-driven air–water two-phase turbulent flows. The incompressible Navier–Stokes equations for both air and water sides have been solved simultaneously using an arbitrary Lagrangian–Eulerian (ALE) method with boundary-fitted moving grids. Finite difference schemes were adopted for the computation of spatial derivatives. The periodic boundary condition was applied in the lateral directions, and the slip condition is applied to the top and bottom boundaries. Initially, the lower water side was static and the free surface was flat, while a wall-bounded turbulent air flow developed for a flat and rigid surface was imposed in the upper air side. The wind speed was comparatively low (approximately $5 \, \mathrm{m \, s^{-1}}$) so that no intensive wave breaking occurs. The DNS were performed for the time integration period of 7 seconds to examine growth of gravity–capillary waves with wavelength less than approximately 0.07 m.

Growth of wind waves was simulated for two values of the surface tension: the value for water and half of that. The results show that the significant waves for the smaller surface tension grow faster, and their wave height becomes higher than that for the larger surface tension. Although wind waves were not well captured during the first 1 second in the present DNS results owing to the initial impact of imposing the wall-bounded turbulent air flow on the air–water interface, the initial wave development is not critical for faster wave growth for the case of smaller surface tension. This is supported by the result that the wave growth speed is increased when the surface tension is suddenly reduced from the wind

waves at $t = 4.0$ s developed with the large surface tension. The effect of surface tension reduction on the wave height has also been confirmed by the wave height measurements in a small wind-wave tank (Appendix A).

The growth of wind waves has been also analysed by the wave height spectra. For both surface tension cases, the spectra grow around the wavenumber for the weakly nonlinear Kelvin–Helmholtz instability for finite amplitude waves in the early growth period. After that, the spectra broaden for both low wavenumbers (gravity waves) and high wavenumbers (capillary waves), having a peak on the low-wavenumber side. The broadening of the wave height spectra is consistent with the harmonic resonance, which forms ripple-like capillary waves. The spectrum also shows that when the surface tension is reduced, a bump at the resonant capillary wave scale moves to higher wavenumber and becomes smaller, indicating that the resonant capillary waves become shorter and weaker.

The numerical convergence of the DNS results is discussed in Appendix C. At the present grid resolution, the temporal variations of the significant wave height and wavelength and the wave height spectrum are weakly dependent on the resolution. However, the resolution dependence is smaller than the difference due to the surface tension reduction. Therefore, the DNS results under the present computational condition are enough to discuss the effects of surface tension reduction.

The temporal variations of wave energy show that the potential energies due to gravity and surface tension are comparable during the early growth period. After this period, the potential energy due to gravity increases rapidly, whereas that due to surface tension remains almost constant. The surface tension reduction results in the increase in the potential energy due to gravity and the decrease in that due to surface tension. The results also show that the growth of the potential energy due to gravity is faster for the smaller surface tension.

The energy flux from air to water has also been investigated to understand the faster growth. The energy flux due to the normal stress, which contributes to wave growth, becomes larger due to the surface tension reduction. The surface tension reduction also causes the decrease in the energy dissipation in the water side. The relationship between the energy flux and the temporal wave-energy change shows that the rapid increase of the wave energy is attributed to the balance between energy flux from the air flow and energy dissipation in the water. The energy flux and energy dissipation filtered for gravity and capillary wave scales show that the energy flux from the air flow is received mostly at the gravity wave scales, and the energy dissipation in the water occurs mostly at the capillary wave scales. This indicates that there is an energy transfer mechanism from the gravity wave scales to the capillary wave scales. The energy dissipation for the capillary wave scales becomes smaller due to the surface tension reduction. This means that the energy transfer from the gravity wave scales to the capillary wave scales decreases due to the surface tension reduction. The analysed results also show that the energy flux due to the tangential stress, i.e. the energy source of shear-induced turbulence, is smaller than the energy dissipation. This suggests that the wave energy due to the normal stress at the gravity wave scales is partially transferred to smaller scales by resonant wave interactions and dissipated at the capillary wave scales. In conclusion, the significant gravity waves receive kinetic energy from the air side with contributions of form drag, and the energy is partially transferred to the capillary waves and dissipated by the viscosity of water. When the surface tension decreases, the energy transfer to the capillary wave scales decreases, and the significant waves retain more energy, resulting in the faster growth of the wave height. The scalar transfer across the air–water interface has been discussed further based on the DNS results.

The scalar transfer coefficient (scalar transfer velocity) for the gas absorption decreases due to the surface tension reduction. The decrease in scalar transfer coefficient cannot be explained by the difference of the interface surface area expansion because the influence of the surface tension reduction on the surface area is negligibly small. Since the turbulent scalar flux and the vorticity fluctuation in the water side becomes smaller due to the surface tension reduction, the decrease in the transfer coefficient is caused by the suppression of turbulence under the interface, particularly turbulence associated with streamwise vortices. The suppression of turbulence can be attributed to the decrease of the friction drag, which drives the shear layer beneath the interface.

Author ORCIDs.
Keigo Matsuda https://orcid.org/0000-0001-9602-4565;
Naohisa Takagaki https://orcid.org/0000-0002-9672-0920;
Ryo Onishi https://orcid.org/0000-0001-9250-0712.

Appendix A. Comparison with wind-wave tank experiments

Laboratory experiments have been conducted to examine the DNS results, in which the wave height becomes higher due to the uniform surface tension reduction. Figure 16 shows a schematic diagram of the experimental apparatus. The experiments were conducted using a small recirculation wind-wave tank (length 1.05 m, width 0.20 m and depth 0.05 m) located in a wind tunnel (Nagata, Sakai & Komori 2007) (length 5.0 m, width 0.30 m and height 0.30 m). A straightened air flow was introduced over the wind-wave tank. The water surface was open to the air flow only at the central test section (length 0.90 m and width 0.09 m) of the tank. The surface water flow induced by the wind shear recirculated through the covered side sections so that a counter-flow was avoided in the lower part of the central test section. A wave absorber was fixed at the end of the test section to prevent the reflection of wind waves and counter-flow. The water-level fluctuation was measured using a capacitance-type displacement meter (Iwatsu Electric Co. Ltd, ST-3572) capable of non-contact measurement. The probe (Iwatsu Electric Co. Ltd, ST-0717A) was set at fetch length $x = 0.70$ m and elevation 0.0020 m or 0.0030 m above the static water level. The sampling time and frequency were 300 s and 1000 Hz, respectively. The measurements were conducted for five cases of the free-stream wind speed U_∞ between 1 and $6 \, \mathrm{m \, s^{-1}}$. In order to quantify the wave height, significant waves were identified using the zero-up crossing method.

Liquids used in the experiments were filtered tap water and two aqueous solutions of ethanol and glycerine. Table 1 shows the surface tension σ and the viscosity μ of each solution. The surface tension of the 30 wt% ethanol solution was approximately half that of the filtered tap water. However, the viscosity of the aqueous ethanol solution was approximately twice that of the filtered tap water. Thus the concentration of the aqueous glycerine solution was adjusted to approximately 30 wt% so that the viscosity was close to the aqueous ethanol solution while the surface tension remained close to the filtered tap water.
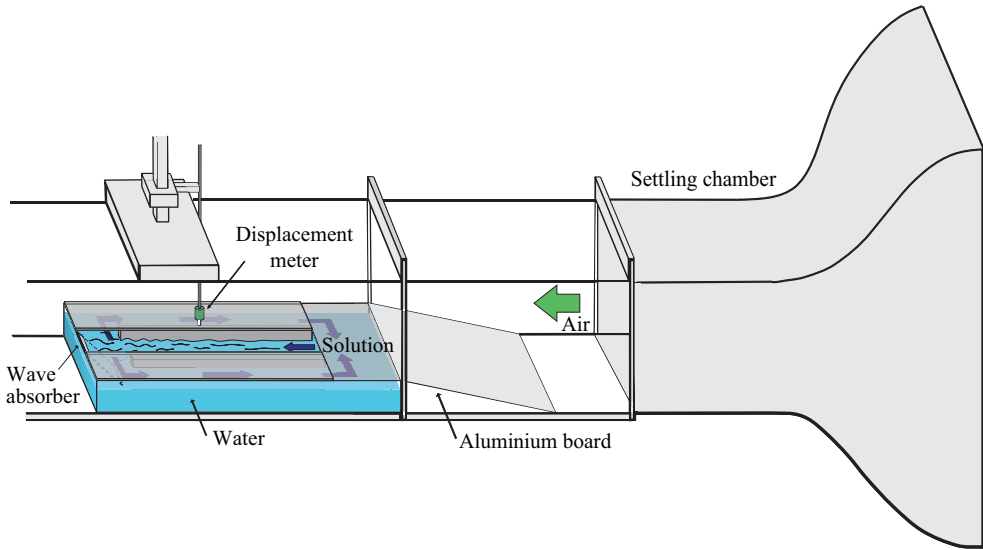
Figure 16. Schematic diagram of the experimental set-up: a small wind-wave tank placed in a wind tunnel, and the water-level fluctuation measurement system.

Solution	σ (10^{-3} N m^{-1})	μ (10^{-3} Pa s)
Filtered tap water	72.0	0.95
Ethanol solution	36.3	2.12
Glycerine solution	69.0	2.41

Table 1. Measured values of surface tension σ and dynamic viscosity μ.

Figure 17 shows the measurements of the significant wave height H_s with the free-stream wind speed U_∞, for the filtered tap water and two aqueous solutions of ethanol and glycerine. When the wind speed U_∞ is higher than 5 m s^{-1}, the significant wave height of the aqueous ethanol solution is larger than that of the aqueous glycerine solution. The difference in the significant wave height is due to the difference in surface tension and not to the difference in viscosity because the significant wave height for the aqueous glycerine solution is almost the same as that of the filtered tap water with the half viscosity at $U_\infty > 5$ m s^{-1}. Paquier *et al.* (2015, 2016) investigated the effect of viscosity on the wind waves experimentally, and reported the presence of the 'wrinkle regime' under large viscosity or weak wind conditions, and the transitions to the regular wave regime under small viscosity or strong wind speed conditions. For $\nu \approx 1.0$–2.0×10^{-6} m^2 s^{-1}, the winkle regime should be observed for approximately $u_{*a} \lesssim 0.19$–0.21 m s^{-1} or $U_\infty \lesssim 3.6$–4.0 m s^{-1}. Thus the difference in the effect of surface tension reduction between low and high wind speed could be due to the difference in the wave regimes. Note that apparently, from the visualisation in figure 2, the wind waves obtained by the DNS are in the regular wave regime.

The experimental condition for the filtered tap water for $U_\infty \approx 5$ m s^{-1} approximately corresponds to the DNS condition $\sigma = 1.0\sigma_w$, where the viscosity was set to $\nu = \nu_w$ and the free-stream wind speed was $U_\infty \approx 5.2$ m s^{-1}. Here, we have performed the DNS
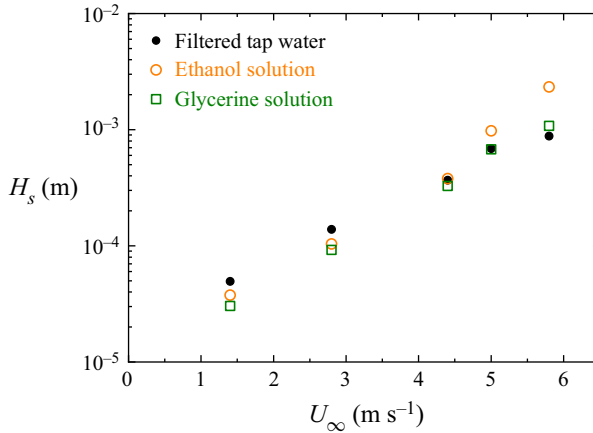
960 A22-24

Figure 17. Significant wave height H_s against free-stream wind speed U_∞.

for additional cases for the aqueous ethanol and glycerine solutions. For the case of the aqueous ethanol solution, the surface tension and the kinematic viscosity were set to $\sigma = 0.5\sigma_w$ and $\nu = 2.0\nu_w$, respectively, and for the aqueous glycerine solution, $\sigma = 1.0\sigma_w$ and $\nu = 2.0\nu_w$, respectively. Other computational conditions were the same as those in § 2.2. Figure 18 shows the temporal variations of the significant wave height H_s, for the cases of the filtered tap water ($\sigma = 1.0\sigma_w$, $\nu = 1.0\nu_w$), the aqueous ethanol solution ($\sigma = 0.5\sigma_w$, $\nu = 2.0\nu_w$), and the aqueous glycerine solution ($\sigma = 1.0\sigma_w$, $\nu = 2.0\nu_w$). To compare the DNS results with the laboratory measurements, we estimate the wave growth time t in the DNS that corresponds to the fetch $x = 0.7$ m in the wind wave tank. According to the fetch law (e.g. Wilson 1965), the fetch is formulated as the function of a wave velocity $\mathcal{C}_s$, which is defined as $\mathcal{C}_s \equiv \sqrt{gL_s/2\pi + 2\pi\gamma/L_s}$ for deep-water gravity–capillary waves with wavelength L_s. This suggests that the significant wave velocity $\mathcal{C}_s$ or wavelength L_s is a suitable parameter for comparison between the DNS results and laboratory measurements. At the fetch $x = 0.7$ m, the measured values of the wave velocity and the wavelength are $\mathcal{C}_s = 0.29$ m s^{-1} and $L_s = 0.033$ m, respectively. In figure 3(b), the significant wavelength obtained by the DNS is close to the measured value for 3 s $\lesssim t \lesssim 4$ s. We have also confirmed that the significant wave velocity averaged over the period $3 \leq t \leq 4$ s is $\mathcal{C}_s = 0.279$ m s^{-1}, close to the laboratory measurement. For the half surface tension case, $\mathcal{C}_s$ can be smaller than the filtered tap water case but its effect on $\mathcal{C}_s$ is smaller than 6 % for the measured wavelength. In the growth stage 3 s $\lesssim t \lesssim 4$ s, the DNS in figure 18 well support the experimental results that the homogeneous surface tension reduction enhances the wave height even when the viscosity is doubled, and the viscosity effect on the wave growth is smaller than the surface tension effect. It is also observed that the wave heights in the DNS results are higher than the measured values. This could be due to the difference in the friction velocity, which was not measured in the experiments. Thus we do not compare the DNS results with the laboratory measurements quantitatively. It would be also interesting to note the viscosity effects of surface tension reduction on wind-wave growth. However, we omit detailed discussion about the sensitivity to the viscosity because it is beyond the scope of this paper.
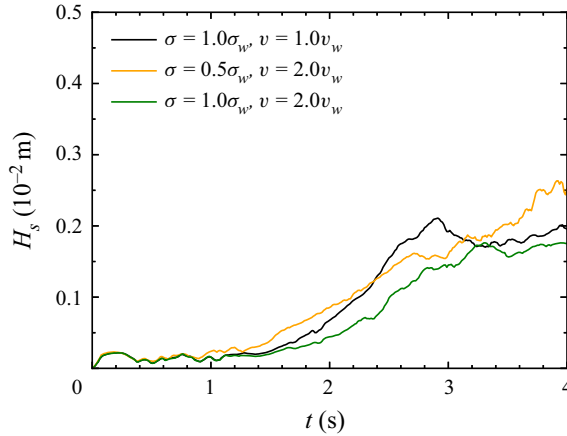
Figure 18. Temporal variations of significant wave height H_s obtained by DNS for the filtered tap water ($\sigma = 1.0\sigma_w$, $\nu = 1.0\nu_w$), the aqueous ethanol solution ($\sigma = 0.5\sigma_w$, $\nu = 2.0\nu_w$), and the aqueous glycerine solution ($\sigma = 1.0\sigma_w$, $\nu = 2.0\nu_w$).

Appendix B. Interface curvature

The interface curvature κ is defined as the divergence of the normal vector on the interface, $\kappa = -\nabla_\Gamma \cdot \boldsymbol{n}$, where $\boldsymbol{n}$ is the unit normal vector to the interface, and ∇_Γ denotes the divergence operator in the interface. To compute the curvature κ, we consider the generalised coordinates (ξ_1, ξ_2, ξ_3) instead of the Cartesian coordinates (x_1, x_2, x_3). In the generalised coordinates, the interface Γ is defined as the surface where ξ_3 equals a constant value ξ_Γ, and the curvature κ is given by the derivative of $\boldsymbol{n}$ in the ξ_1 and ξ_2 directions:

$$\kappa = -\left[\frac{\boldsymbol{a}_2 \times \boldsymbol{n}}{|\boldsymbol{a}_1 \times \boldsymbol{a}_2|} \frac{\partial \boldsymbol{n}}{\partial \xi_1} + \frac{\boldsymbol{n} \times \boldsymbol{a}_1}{|\boldsymbol{a}_1 \times \boldsymbol{a}_2|} \frac{\partial \boldsymbol{n}}{\partial \xi_2} \right], \tag{B1}$$

where $\boldsymbol{a}_i \equiv (\partial x_j / \partial \xi_i)\, \boldsymbol{e}_j$, and $\boldsymbol{e}_j$ is the basis vector of the Cartesian coordinate. The normal vector is given by $\boldsymbol{n} = (\boldsymbol{a}_1 \times \boldsymbol{a}_2)/|\boldsymbol{a}_1 \times \boldsymbol{a}_2|$. The relationship $\boldsymbol{n} \cdot \boldsymbol{a}_1 = \boldsymbol{n} \cdot \boldsymbol{a}_2 = 0$ yields

$$\kappa = \frac{h_{11}g_{22} + h_{22}g_{11} - 2h_{12}g_{12}}{g_{11}g_{22} - g_{12}g_{12}}, \tag{B2}$$

where $h_{ij} \equiv \boldsymbol{n} \cdot \partial \boldsymbol{a}_j / \partial \xi_i$ and $g_{ij} \equiv \boldsymbol{a}_i \cdot \boldsymbol{a}_j$.

Appendix C. Numerical convergence

The numerical convergence of the DNS results has been examined by changing the streamwise resolution. The DNS results obtained for $M_1 = 400$, where M_1 is the number of grid points, were compared with the additional DNS results for $M_1 = 200$, 300 and 532. The grid spacing was scaled for the fixed domain size. Figure 19 shows the vertical profiles of the mean streamwise air velocity U_1 and the r.m.s. value of the streamwise air velocity fluctuations u' of the initial wall-bounded turbulent flows obtained for different resolutions. The vertical axes are normalised by u_{*a}, i.e. $U_1^+ = U_1/u_{*a}$ and $u'^+ = u'/u_{*a}$. The horizontal axis is the vertical position in the viscous unit $z^+ = z u_{*a}/\nu_a$. As shown in figure 19, for both U_1^+ and u'^+, the profiles for different resolutions are well converged.

Figure 20 shows the temporal variations of significant wave height and wavelength, H_s and L_s, respectively, for different resolutions. The growth of H_s for $M_1 = 200$ is slower
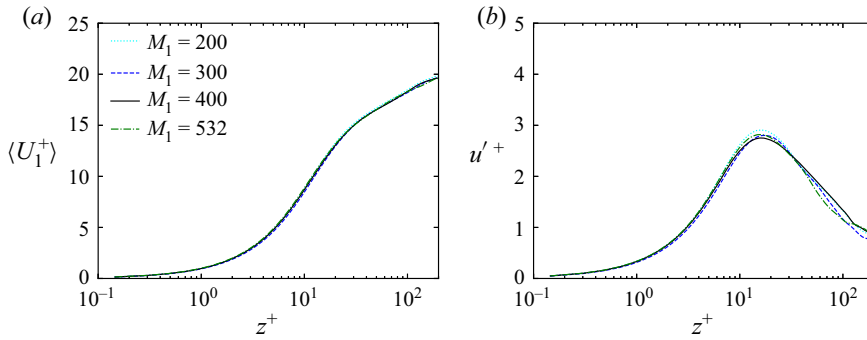
960 A22-26

Figure 19. Vertical profile of (*a*) mean streamwise air velocity U_1^+, and (*b*) streamwise air velocity fluctuation u'^+, of the initial wall-bounded turbulent flows obtained with different resolutions.
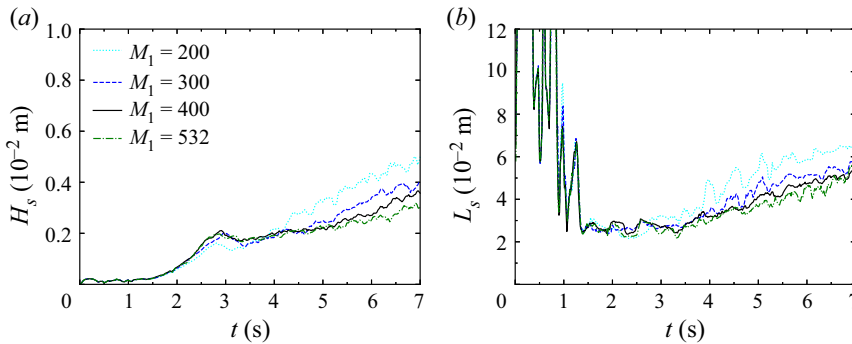

Figure 20. Temporal variations of (*a*) significant wave height H_s, and (*b*) significant wavelength L_s, obtained for $\sigma = 1.0\sigma_w$ with different resolutions.

than the growth for higher resolution, particularly for $t < 3$ s, but the wave growths for the other resolutions are well converged. For $M_1 \geq 300$, the difference in H_s between the different resolutions increases gradually with time. The small difference between the different resolution cases for $M_1 \geq 300$ is smaller than the difference due to the surface tension reduction. The convergence is similarly confirmed for temporal variation of L_s.

Figure 21 shows the time-averaged wave height spectra for the cases $\sigma = 1.0\sigma_w$ and $\sigma = 0.5\sigma_w$ obtained for different resolutions. As expected from the temporal variations of the significant wave height and wavelength, the wave spectra for low wavenumbers $(k_1 < k_m)$ are well converged. For high wavenumbers $(k_1 > k_m)$, the wave spectra are almost converged. We can still see weak dependence on the resolution, but the resolution dependence is sufficiently smaller than the difference due to the surface tension reduction. Thus the present DNS are sufficiently converged over all the scales to discuss the surface tension effect.

Appendix D. Wave growth rate

The wave growth was often evaluated by using the wave growth rate (Donelan *et al.* 2006). Here, the wave growth rate in our DNS is compared with the measurements in the literature (Plant 1982). We use the wave growth rate β defined as

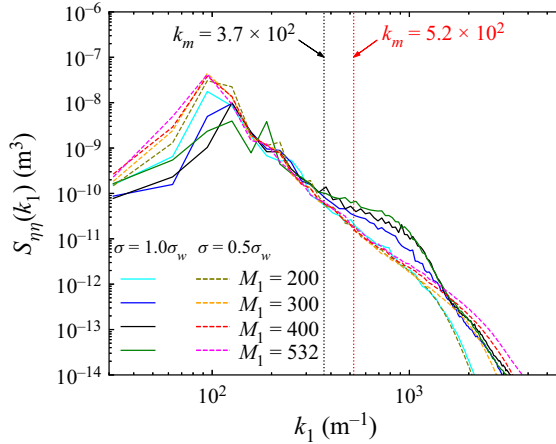$$\beta \equiv \frac{1}{E} \frac{\mathrm{d}E}{\mathrm{d}t}, \tag{D1}$$

Figure 21. Wave height spectra averaged for the period $4.0 < t \le 7.0\,\mathrm{s}$, obtained for $\sigma = 1.0\sigma_w$ and $\sigma = 0.5\sigma_w$ with different resolutions. Vertical dotted lines in black and red are the wavenumbers k_m for $\sigma = 1.0\sigma_w$ and $\sigma = 0.5\sigma_w$, respectively.

where E is the total wave energy. As described in § 3.1, it is difficult to extract the kinetic energy of the wave motion from the total kinetic energy including the turbulent kinetic energy. Here, we assume again that the kinetic energy of the wave motion is equivalent to the potential energy, and the wave growth rate is obtained from $\beta = \mathrm{d}\log(E_g + E_s)/\mathrm{d}t$. Figure 22 shows β calculated by fitting a linear function to $\log(E_g + E_s)$ for every $0.5\,\mathrm{s}$. The grey symbols are the measurements summarised in figure 2 of Plant (1982). The solid and dashed lines are the relations obtained by Plant (1982) and given by

$$\beta = \frac{(0.04 \pm 0.02)u_{*a}^2\omega\cos\theta}{\mathcal{C}^2}, \tag{D2}$$

where u_{*a} is the friction velocity on the air side, $\omega = 2\pi f$ is the radian wave frequency, θ is the angle between wind and wave directions, and $\mathcal{C}$ is the phase speed. As shown in figure 22(a), the relationship between β/f and $u_{*a}/\mathcal{C}$ agrees with the measurements. Note that $\rho_a u_{*a}^2$ is the sum of form and friction drags, D_p and D_f, respectively, while u_{*a} in (D2) is relevant to the contribution of the form drag D_p (Melville & Fedorov 2015). Since the energy flux due to the normal stress satisfies $Q_{na} \approx \mathcal{C}D_p$, the wave growth rate β/f should be compared with $Q_{na}/\rho_a\mathcal{C}^3$. In figure 22(b), the wave growth rate obtained from our DNS results is plotted against $Q_{na}/\rho_a\mathcal{C}^3$, and the correlation with $Q_{na}/\rho_a\mathcal{C}^3$ is better than that with $(u_{*a}/\mathcal{C})^2$.

Appendix E. Scalar budget equation

To evaluate the scalar transfer below the moving interface, we consider the continuous surface $\Gamma_{z_{g0}}$. Therefore, we consider the coordinate transform from Cartesian coordinates (x_1, x_2, x_3) to the boundary-fitted coordinates $(\varXi_1, \varXi_2, \varXi_3)$. The computational grids are fixed on $(\varXi_1, \varXi_2, \varXi_3)$, and $(\varXi_1, \varXi_2, \varXi_3)$ is equivalent to (x_1, x_2, x_3) at $t = 0$. In the boundary-fitted coordinate, the surface $\Gamma_{z_{g0}}$ is represented by $\varXi_3 = z_{g0}$. The scalar transport equation in the boundary-fitted coordinate can be described as

$$\frac{\partial C|\boldsymbol{J}|}{\partial t} + \frac{\partial C(U_j - V_j)K_{jk}}{\partial \varXi_k} = \frac{\partial}{\partial \varXi_k}\left(D\frac{\partial C}{\partial x_j}K_{jk}\right), \tag{E1}$$
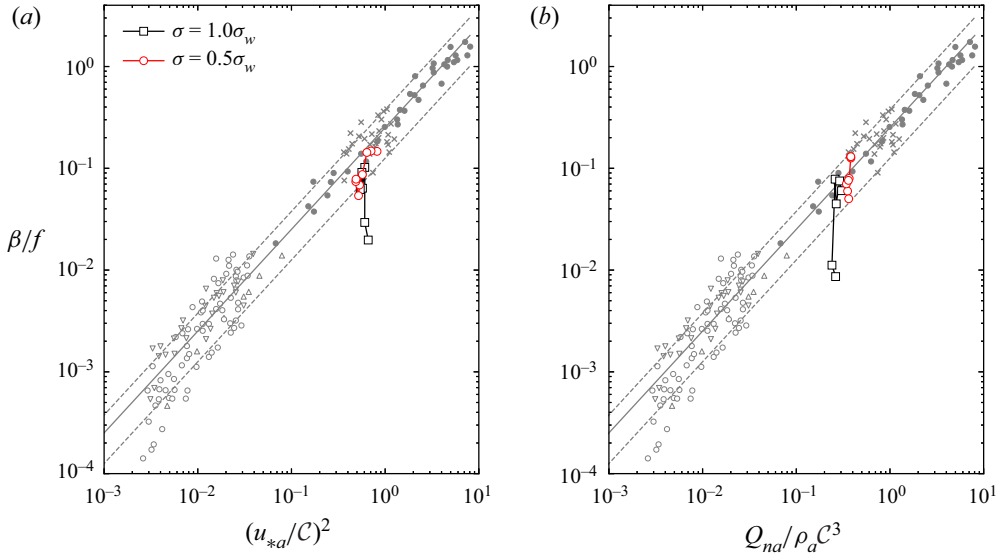
Figure 22. Wave growth rate β normalised by the wave frequency f against (a) $(u_{*a}/\mathcal{C})^2$, and (b) $Q_{na}/\rho_a\mathcal{C}^3$. Here, u_{*a}^2 and Q_{na} are temporally averaged for every $0.5\,\text{s}$ after $t = 4.0\,\text{s}$ for $\sigma = 1.0\sigma_w$ (black open squares), and $t = 3.0\,\text{s}$ for $\sigma = 0.5\sigma_w$ (red open circles). We obtain β by linear fitting to $\log(E_g + E_s)$ for every $0.5\,\text{s}$ in the corresponding period. The other symbols are the measurements summarised in figure 2 of Plant (1982). The solid and dashed lines represent (D2).

where $\boldsymbol{J}$ is the Jacobian matrix $\boldsymbol{J} = \partial(x_1, x_2, x_3)/\partial(\varXi_1, \varXi_2, \varXi_3)$, $|\boldsymbol{J}|$ is the determinant of $\boldsymbol{J}$, K_{ij} is the (i, j) component of the adjugate matrix of $\boldsymbol{J}$, and V_i is the ith component of the velocity of grid points on the boundary-fitted coordinate. Since the boundary-fitted coordinate deforms only in the x_3 direction, the components of the Jacobian matrix are $J_{11} = J_{22} = 1$, $J_{13} = \partial z_g/\partial x_1$, $J_{23} = \partial z_g/\partial x_2$, $J_{33} = \partial z_g/\partial z_{g0}$ and $J_{12} = J_{21} = J_{31} = J_{32} = 0$. Thus the determinant becomes $|\boldsymbol{J}| = |J_{33}|$, and K_{ij} is given by $K_{11} = K_{22} = J_{33}$, $K_{13} = -J_{13}$, $K_{23} = -J_{23}$, $K_{33} = 1$ and $K_{12} = K_{21} = K_{31} = K_{32} = 0$. The components of the velocity of the boundary-fitted coordinate are $V_1 = V_2 = 0$ and $V_3 = \partial z_g/\partial t$. Applying the integral over the volume $0 \leq \varXi_1 \leq L_1$, $0 \leq \varXi_2 \leq L_2$ and $-2\delta \leq \varXi_3 \leq z_{g0}$ in the boundary-fitted coordinate, and using the Gauss divergence theorem for the advection and diffusion terms, we obtain

$$\frac{\mathrm{d}\chi(z_{g0})}{\mathrm{d}t} = \left\langle D\frac{\partial C}{\partial x_j}K_{j3}\right\rangle_{z_{g0}} - \left\langle C(U_j - V_j)K_{j3}\right\rangle_{z_{g0}}, \tag{E2}$$

where $\chi(z_{g0})$ is given by (3.18). In the boundary-fitted coordinate, $\chi(z_{g0})$ and the bracket $\langle\cdot\rangle_{z_{g0}}$ are described as $\chi(z_{g0}) = (1/L_1L_2)\int_0^{L_1}\int_0^{L_2}\int_{-2\delta}^{z_{g0}} C\,|\boldsymbol{J}|\,\mathrm{d}\varXi_1\,\mathrm{d}\varXi_2\,\mathrm{d}\varXi_3$ and $\langle A\rangle_{z_{g0}} = (1/L_1L_2)\int_0^{L_1}\int_0^{L_2} A(\varXi_3 = z_{g0})\,\mathrm{d}\varXi_1\,\mathrm{d}\varXi_2$ for a given function A, respectively. By using the scalar concentration fluctuation $c = C - \langle C\rangle_{z_{g0}}$ and the vertical fluid velocity relative to the velocity of boundary-fitted coordinate w_3, the full budget equation is yielded as

$$\frac{\mathrm{d}\chi(z_{g0})}{\mathrm{d}t} = F_{diff} - \langle cw_3\rangle_{z_{g0}} - \langle C\rangle_{z_{g0}}\langle w_3\rangle_{z_{g0}}, \tag{E3}$$

where F_{diff} is given by (3.19). Note that the third term vanishes because $\langle w_3\rangle_{z_{g0}}$ vanishes.

REFERENCES

BONTOZOGLOU, V. & HANRATTY, T.J. 1990 Capillary-gravity Kelvin–Helmholtz waves close to resonance. *J. Fluid Mech.* **217**, 71–91.

BUCKLEY, M.P., VERON, F. & YOUSEFI, K. 2020 Surface viscous stress over wind-driven waves with intermittent airflow separation. *J. Fluid Mech.* **905**, A31.

CAULLIEZ, G. 2013 Dissipation regimes for short wind waves. *J. Geophys. Res.* **118**, 672–684.

CHEN, B. & SAFFMAN, P.G. 1979 Steady gravity-capillary waves on deep water. I. Weakly nonlinear waves. *Stud. Appl. Maths* **60**, 183–210.

CHEN, B. & SAFFMAN, P.G. 1980 Steady gravity-capillary waves on deep water. II. Numerical results for finite amplitude. *Stud. Appl. Maths* **62**, 95–111.

DEIKE, L., MELVILLE, W.K. & POPINET, S. 2016 Air entrainment and bubble statistics in breaking waves. *J. Fluid Mech.* **801**, 91–129.

DEIKE, L., POPINET, S. & MELVILLE, W.K. 2015 Capillary effects on wave breaking. *J. Fluid Mech.* **769**, 541–569.

DONELAN, M.A., BABANIN, A.V., YOUNG, I.R. & BANNER, M.L. 2006 Wave-follower field measurements of the wind-input spectral function. Part II: parameterization of the wind input. *J. Phys. Oceanogr.* **36**, 1672–1689.

FEDOROV, A.V., MELVILLE, W.K. & ROZENBERG, A. 1998 An experimental and numerical study of parasitic capillary waves. *Phys. Fluids* **10**, 1315–1323.

FERZIGER, J.H., PERIĆ, M. & STREET, R.L. 2020 *Computational Methods for Fluid Dynamics*, 4th edn. Springer Nature Switzerland AG.

GRARE, L., PEIRSON, W.L., BRANGER, H., WALKER, J.W., GIOVANANGELI, J.-P. & MAKIN, V. 2013 Growth and dissipation of wind-forced, deep-water waves. *J. Fluid Mech.* **722**, 5–50.

HOLTHUIJSEN, L. 2007 *Waves in Oceanic and Coastal Waters*. Cambridge University Press.

HUNG, L.-P. & TSAI, W.-T. 2009 The formation of parasitic capillary ripples on gravity–capillary waves and the underlying vortical structures. *J. Phys. Oceanogr.* **39**, 263–289.

IMASATO, N. 1976 Some characteristics of the development process of the wind–wave spectrum. *J. Oceanogr. Soc. Japan* **32**, 21–32.

IWANO, K., TAKAGAKI, N., KUROSE, R. & KOMORI, S. 2013 Mass transfer velocity across the breaking air–water interface at extremely high wind speeds. *Tellus* B **65** (1), 21341.

JÄHNE, B., MÜNNICH, K.O. & SIEGENTHALER, U. 1979 Measurements of gas exchange and momentum transfer in a circular wind–water tunnel. *Tellus* **31**, 321–329.

JEFFREYS, H. 1925 On the formation of water waves by wind. *Proc. R. Soc. Lond.* A **107**, 189–206.

KAWAI, S. 1979 Discussion on the critical wind speed for wind–wave generation on the basis of shear-flow instability theory. *J. Oceanogr. Soc. Japan* **35**, 179–186.

KOMORI, S., KUROSE, R., IWANO, K., UKAI, T. & SUZUKI, N. 2010 Direct numerical simulation of wind-driven turbulence and scalar transfer at sheared gas–liquid interfaces. *J. Turbul.* **11**, N32.

KOMORI, S., NAGAOSA, R. & MURAKAMI, Y. 1993*a* Turbulence structure and mass transfer across a sheared air–water interface in wind-driven turbulence. *J. Fluid Mech.* **249**, 161–183.

KOMORI, S., NAGAOSA, R., MURAKAMI, Y., CHIBA, S., ISHII, K. & KUWAHARA, K. 1993*b* Direct numerical simulation of three-dimensional open-channel flow with zero-shear gas–liquid interface. *Phys. Fluids* **5**, 115–125.

KUROSE, R., TAKAGAKI, N., KIMURA, A. & KOMORI, S. 2016 Direct numerical simulation of turbulent heat transfer across a sheared wind-driven gas–liquid interface. *J. Fluid Mech.* **804**, 646–687.

LIN, M.-Y., MOENG, C.-H., TSAI, W.-T., SULLIVAN, P.P. & BELCHER, S.E. 2008 Direct numerical simulation of wind–wave generation processes. *J. Fluid Mech.* **616**, 1–30.

MELVILLE, W.K. & FEDOROV, A.V. 2015 The equilibrium dynamics and statistics of gravity-capillary waves. *J. Fluid Mech.* **767**, 449–466.

MILES, J.W. 1957 On the generation of surface waves by shear flows. *J. Fluid Mech.* **3**, 185–204.

MILES, J.W. 1959 On the generation of surface waves by shear flows. Part 3. Kelvin–Helmholtz instability. *J. Fluid Mech.* **6**, 583–598.

MILES, J.W. 1986 Weakly nonlinear Kelvin–Helmholtz waves. *J. Fluid Mech.* **172**, 513–529.

MILES, J.W. 1993 Surface-wave generation revisited. *J. Fluid Mech.* **256**, 427–441.

MITSUYASU, H. & HONDA, T. 1986 The effect of surfactant on certain air–sea interaction phenomena. In *Wave Dynamics and Radio Probing of the Ocean Surface* (ed. O.M. Phillips & K. Hasselmann), pp. 95–115. Springer.

MOSTERT, W. & DEIKE, L. 2020 Inertial energy dissipation in shallow-water breaking waves. *J. Fluid Mech.* **890**, A12.

NAGATA, K., SAKAI, Y. & KOMORI, S. 2007 Momentum and heat transfer in turbulent boundary layers with external grid turbulence. In *Advances in Turbulence XI* (ed. J.M.L.M. Palma & A. Silva Lopes), pp. 444–446. Springer.

PAQUIER, A., MOISY, F. & RABAUD, M. 2016 Viscosity effects in wind wave generation. *Phys. Rev. Fluids* **1**, 083901.

PAQUIER, A., MOISY, F. & RABAUD, M. 2015 Surface deformations and wave generation by wind blowing over a viscous liquid. *Phys. Fluids* **27**, 122103.

PERRARD, S., LOZANO-DURÁN, A., RABAUD, M., BENZAQUEN, M. & MOISY, F. 2019 Turbulent windprint on a liquid surface. *J. Fluid Mech.* **873**, 1020–1054.

PHILLIPS, O.M. 1957 On the generation of waves by turbulent wind. *J. Fluid Mech.* **2**, 417–445.

PIERSON, W.J. JR. 1954 An interpretation of the observable properties of 'sea' waves in terms of the energy spectrum of the Gaussian record. *EOS Trans. AGU* **35** (5), 747–757.

PLANT, W.J. 1982 A relationship between wind stress and wave slope. *J. Geophys. Res.* **87** (C3), 1961–1967.

SCOTT, J.C. 1972 The influence of surfactant-active concentration on the initiation of wind waves. *J. Fluid Mech.* **56**, 591–606.

SULLIVAN, P.P. & MCWILLIAMS, J.C. 2010 Dynamics of winds and currents coupled to surface waves. *Annu. Rev. Fluid Mech.* **42**, 19–42.

TAKAGAKI, N., KUROSE, R., TSUJIMOTO, Y., KOMORI, S. & TAKAHASHI, K. 2015 Effects of turbulent eddies and Langmuir circulations on scalar transfer in a sheared wind-driven liquid flow. *Phys. Fluids* **27**, 016603.

TAKAGAKI, N., SUZUKI, R., TAKAHATA, S. & KUMAMARU, H. 2020 Effects of air-side freestream turbulence on the development of air–liquid surface waves. *Exp. Fluids* **61**, 136.

TEJADA-MARTÍNEZ, A.E., HAFSI, A., AKAN, C., JUHA, M. & VERON, F. 2020 Large-eddy simulation of small-scale Langmuir circulation and scalar transport. *J. Fluid Mech.* **885**, A5.

TOBA, Y. 1972 Local balance in the air–sea boundary processes. I. On the growth process of wind waves. *J. Oceanogr. Soc. Japan* **28**, 109–120.

TSAI, W.-T. & LIN, M.-Y. 2004 Stability analysis on the initial surface-wave generation within an air–sea coupled shear flow. *J. Mar. Sci. Technol.* **12** (3), 200–208.

VERON, F. & MELVILLE, W.K. 2001 Experiments on the stability and transition of wind-driven water surfaces. *J. Fluid Mech.* **446**, 25–65.

WANNINKHOF, R., ASHER, W.E., HO, D.T., SWEENEY, C. & MCGILLIS, W.R. 2009 Advances in quantifying air–sea gas exchange and environmental forcing. *Annu. Rev. Mar. Sci.* **1** (1), 213–244.

WILSON, B.W. 1965 Numerical prediction of ocean waves in the North Atlantic for December, 1959. *Dtsch. Hydrogr. Z.* **18**, 114–130.

WU, J. & DEIKE, L. 2021 Wind wave growth in the viscous regime. *Phys. Rev. Fluids* **6**, 094801.

YANG, D. & SHEN, L. 2011 Simulation of viscous flows with undulatory boundaries: part II. Coupling with other solvers for two-fluid computations. *J. Fluid Mech.* **230**, 5510–5531.

ZAVADSKY, A. & SHEMER, L. 2017 Water waves excited by near-impulsive wind forcing. *J. Fluid Mech.* **828**, 459–495.

ZONTA, F., SOLDATI, A. & ONORATO, M. 2015 Growth and spectra of gravity-capillary waves in countercurrent air/water turbulent flow. *J. Fluid Mech.* **777**, 245–259.